TÉCNICO LISBOA

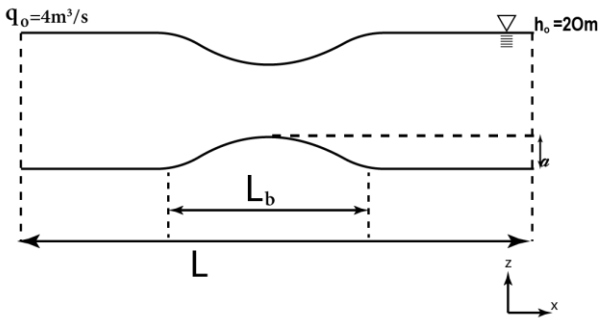

A discontinuous Galerkin method for solving the shallow water equations

Daniela Vignali

Thesis to obtain the Master of Science Degree in

Energy engineering and management

Supervisor: Prof. João Carlos de Campos Henriques

Examination Committee

Chairperson: Prof. Edgar Caetano Fernandes
Supervisor: Prof. João Carlos de Campos Henriques
Member of the Committee: Prof. Jose´ Maria Campos da Silva Andre´

May 2023

Declaration

I declare that this document is an original work of my own authorship and that it fulfills all the requirements of the Code of Conduct and Good Practices of the Universidade de Lisboa.

Acknowledgements

I would like to thank Prof. João Carlos de Campos Henriques for his support, insight and encouragement along this thesis. I am grateful for the advice and love received from my friends, especially Padma, Silvia, Alice C. and Alice B.. This thesis would not have been possible without my family. Even if always distant geographically it gave me an unbelievable help emotionally, spiritually and work-wise.

Abstract

The demand for energy has increased exponentially in many countries around the world. Tidal stream energy is one of the most promising renewable energy sources, due to its predictability, low environmental impact and no occupation of land. However, high investment costs and restricted sites are available, which slow development and improvement. Understanding the resource in the framework of new tidal stream technologies is essential to have a clear view of the power generation available. The shallow water equations have been successfully applied in describing tidal waves and tidal analysis. The shallow water system is a set of hyperbolic partial differential equations. This thesis focuses on developing a numerical model with the Discontinuous Galerkin Method to solve these types of equations. The Discontinuous Galerkin method allows the conservation of mass and momentum on an element basis, and is well suited for unstructured meshes. The conservation of variables guarantees a correct calculation of the flow rate and the momentum flux in the local field and along the water depth. The model has been developed in one-dimensional and two-dimensional versions. One-dimensional results are presented for a bump. The analysis of the error guarantees the accuracy of the solution. The two-dimensional model was used to simulate in a uniform solution which presents good results.

Keywords: Tidal Energy, Shallow Water Equations, Discontinuous Galerkin Method, High-order methods

Resumo

A procura de energia tem aumentado exponencialmente em muitos países do mundo. A energia das correntes marítimas é uma das fontes de energia renovável mais promissoras, devido à sua previsibilidade, baixo impacto ambiental e ausência de ocupação de terras. No entanto, os elevados custos de investimento e a disponibilidade de locais restritos atrasam o seu desenvolvimento e aperfeiçoamento. A compreensão do recurso no âmbito das novas tecnologias de correntes marítimas é essencial para se ter uma visão correcta da produção de energia disponível. As equações de águas pouco profundas têm sido aplicadas com sucesso na descrição das ondas de maré e na análise das marés. O sistema de águas pouco profundas é um conjunto de equações diferenciais parciais hiperbólicas. Esta tese centra-se no desenvolvimento de um modelo numérico com o Método de Galerkin Descontínuo para resolver este tipo de equações. O método de Galerkin Descontínuo permite a conservação da massa e do momento numa base de elementos, e é adequado para malhas não estruturadas. A conservação das variáveis garante um cálculo correcto do caudal e do fluxo de momento no campo local e ao longo da profundidade da água. O modelo foi desenvolvido em versões unidimensionais e bidimensionais. Os resultados unidimensionais são apresentados para um ressalto. A análise do erro garante a exactidão da solução. O modelo bidimensional foi utilizado para simular uma solução uniforme que apresenta bons resultados.

Palavras-Chave: Tidal Energy, Shallow Water Equations, Discontinuous Galerkin Method, Métodos de ordem superior

Contents

List of Figures

List of Acronyms

EMEC	European Marine Energy Centre
LMADT	Linear Momentum Actuator Disc Theory
FEM	Finite Element Method
DG	Discontinuous Galerkin Method

List of Symbols

g Gravity Acceleration

ρ Water Density

m Mass

ζ Surface Perturbation

θ Local Coordinate - Parameterization

Γ^{int} Internal Set of Boundary

Γ^{bc} External Set of Boundary - Boundary Condition

$\mathbf{v} = (u, v)$ Velocity Vector with u on the x-axis and v on the y-axis

$b(x, y)$ Seabed Bathymetry

n Outward Normal

q Conservative Variables

F Flux

H Numerical Flux

s Source

$\hat{\Omega}$ Standard Element

Ω_e General Element

$\boldsymbol{\mathcal{R}}_n(q)$ Residual

ξ, η Coordinates in the Standard Space

ψ Element shape function

J Jacobian matrix

$det\mathbf{J}$ Determinat of the Jacobian matrix

Chapter 1

Introduction

In the past half-century, energy requirements have grown rapidly in many countries all around the globe. Digitization and population growth have been the main drivers in the electricity demand climb. The exploration of renewable energy options is necessary for energy and climate problems, as fossil fuel, related to the CO_2 emissions, and the electricity stability to fill the grid demand. The European Environmental Agency report 'Trends and Projections in Europe 2021' concludes that the European Union succeeded in achieving the climate and energy targets: the greenhouse gas emissions reduction by 20% considering 1990 as the reference scenario, the share of renewable energy increment to 20%, and energy efficiency enrichment by 20%, where the reference scenario is 2007. The following milestone is 2030 when the targets got even more ambitious. Starting with 55% mitigation of the greenhouse gas emissions, 32% increase of renewable energy in the European Union gross final energy consumption, and 32.5% improvement of energy efficiency.
Ocean energy is one of the most promising energy sources to tackle some of these problems. [2] On the other hand, there are consistent concerns about the amount of energy available, the possible causes on biodiversity and the actual energy disposable without environmental threat.

1.1 Tides: generation, distribution and dissipation

Tides occur as a result of a non-uniform gravitational field. They respond under the gravitational forces of the Moon, Sun and other astronomical bodies. On top of this, tides are affected by the presence of continents, variable water depth and seabed shape, which create a more complicated scheme and determine a significant variation in the tidal range around the world. The amplitude can move from less than 1 m in the deep ocean up to 11.7 m in the coastal region as the Bay of Fundy (Canada), or Bristol Channel (UK). This intensified tidal range can also be observed in other coastal regions, where the common characteristic of these locations is the resonant excitation reached by the tides. [32]

Considering only the effect of the Moon and Sun on the ocean, their gravity creates two protrusions on the Earth's surface, as shown in figure 1.1. As known, the Moon has a higher influence on tides than the Sun, approximately 2,18 times more, due to the shorter distance between Earth and Moon. In addition, the declination of the Moon's

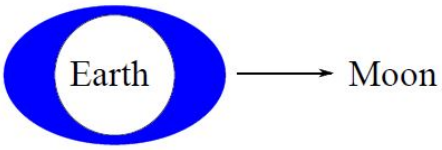

Figure 1.1: Water distribution without continents [52]

orbital plane with respect to the Earth's axis generates diurnal tides at high latitudes, semi-diurnal tides near the equator and in the middle area there are mixed tides; i.e. two tides during the day and significant deviation between a tidal range and the following one. However, the geographical subdivision of the tidal time frame is fragmented by continents generating a more complex distribution, as shown in figure 1.2. [23]

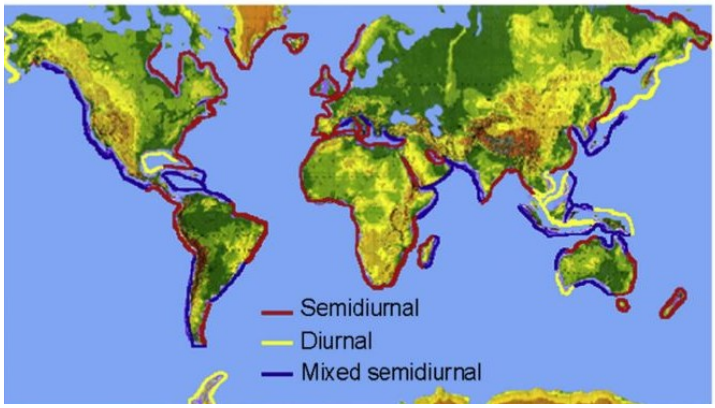

Figure 1.2: Geographical incident of the three types of tides [3]

Tidal progression is structured around the different ocean basins, with greater tidal amplifications at the coastlines. The lines move concentrically forward the amphidromic points, where the tidal range is zero, as shown in figure 2.1. Tides at the coasts are the outcome of the synergy of the harmonic constituent of different tides. [20] Two main mechanisms define the increase in tidal amplitude closer to shore: first, the narrowing of a channel or an estuary, which leads to a concentration of energy in the tide, and second, the magnified intersection between incoming and reflected components of the tide.[20] This natural resonance, with the standing wave shape, is obtained when the width of the continent's coastline is around one-fourth of the tidal mode wavelength. [32]
Tidal currents have a natural dissipation of energy due to the friction force with the rough seabed. It is a considerable amount of energy on the global scale and is estimated to be around 2-3 TW for the principal lunar component M2. This represents the $\frac{2}{3}$ of the global energy dissipation in the tidal force, the remained $\frac{1}{3}$ is assumed to be involved in the internal mixing processes of the deep water.[14, 40]

Tidal streams or tidal currents are flows of ocean water due to the changing tidal level, which embrace large kinetic energy and can be exploited for electricity power generation. Generally, it is possible to extract energy from them near shore, particularly, where there are constrictions, such as channels, islands and passages.

A valuable energy source in the modern power market does not necessarily have to be constant. Although, it has to be reliable, which means being predictable in quantity and time, such as tidal energy, in contrast, other renewable energies follow stochastic patterns, for instance, wind, solar and wave. All renewable energies are intermittent. In the case of tides, discontinuous power production is derived from the natural variation of the resource in time and

the performance of the technology used to produce energy. Beside, tides are cyclical which simplifies high-efficient systems development.

Tidal power has suffered from high investment costs and restricted sites available with adequate tidal ranges or velocities, thus narrowing down its total availability. Further, it has an influence on marine biodiversity. Despite this, recent technological and design developments indicate that the total availability of tidal power might be higher than previously estimated, approximately 1,200 TWh per year. In addition, economic and environmental costs may be brought down to competitive levels. [6, 2]

1.2 Energy extraction

Currently, there are three main options for producing energy from coastal tides: the barrage requires the construction of a dam across a bay or an estuary, in order to exploit the potential energy between the rise and fall of the tides; the tidal turbine involves the deployment of devices to extract energy from tidal streams; the tidal fence is a hybrid between the barrage and the tidal turbine.

Figure 1.3: Type of tidal energy devices [1]

A barrage necessitates a dam to close a restricted natural area to create a basin. The dam typically works in the ebb tide, thus sluice gates are left open to fill the basin during the flood tide and are closed when the high tide is reached. At a certain height difference between the sea and the basin is met, turbines start generating power during the ebb tide and the process is reversed if the barrage works in the flood tide. In addition, this system can generate energy even with both ebb and flood tides, even though it does not provide more energy than the previous modes. Moreover, it needs reversible turbines, but the power production is more consistent in time, raising the capacity factor. However, the actual production of energy can be improved by the introduction of a pumping phase, i.e. in the ebb generation the water is pumped into the basin during the high tide to have a higher water head during the low tide, and in the flood generation, the water is pumped from the basin into the sea. This is the most environmentally impact option of the three available, suffering from invasive civil infrastructure, which leads to high initial investment. The first large-scale tidal power plant was La Rance (France). It has been operating in the dual generation with the pump phase since 1966 with 240 MW of total capacity. Annapolis Royal in Canada has been in operation from 1984 to 2019, with only one turbine of 18 MW in the ebb generation. The last and largest tidal plant was built in South Korea, Sihlwa Basin, in 2011, which had a total capacity of 254 MW in flood generation.

Tidal turbines have an initial concept similar to wind turbines, where they are located in a fluid with a specific layout to minimise interference on each other, are subject to the highest amount of flow and exploit kinetic energy. However, tidal turbines are deployed in water, a fluid 784 times denser than air, which allows the exploitation of slower fluxes, typically from 0.5 m/s up to 6 m/s. They will be further described in chapter 2.1. The European

Marine Energy Centre is located in the Orkney Islands. It is the main European test centre for tidal currents and other ocean energies, which provides facilities for testing the devices and support for installation, maintenance and grid connection [4].

A tidal fence is another form to exploit energy from a tidal stream, which forces the fluid to flow through vertical turbines. At the same time, they do not block the fluid, as a barrage, which is always free to move continuously. On the other hand, the turbines are connected to one another creating a fence structure with only one row, instead of being individually placed as tidal turbines. Therefore, it represents dynamic tidal power, a combination of potential and kinetic energies.

Tidal turbine generally is the most sustainable option out of the three above-mentioned, considering the amount of material used for the construction and the environment and economic impact on the areas. [53]

1.3 Energy potential

The natural dissipation rate does not represent the size of the tidal resource exploitable for human energy production. A way to determine the available energy is based on simplified models of coastal geometries unified with numerical simulation of energy extraction. This method assumes fixed tidal oscillations at an arbitrary distance from the coastal site evaluated and a fixed tidal range. Thus it is legit to assume the existence of an upper limit to the quantity of energy that can be dissipated by combining natural friction and human energy production.[7]

In wind energy, the theoretical upper limit for a wind converter is determined by the Betz limit. The tidal environment has consistent differences from wind. In fact, the Betz model assumes unbounded and incompressible fluid, where the boundaries are infinitely far away from the location examined. Whereas the tidal flow is constrained by the free surface and the seabed, also the free surface variation is an essential characteristic of the tidal system. Therefore, the Betz limit is incompatible with the extraction of tidal energy, considering the tidal environment does not satisfy the method's assumption. Nonetheless, it can be considered a valuable option for resource assessment to guarantee a reasonable practical limit. At the same time, there are studies regarding an equivalent parameter for tidal applications of the Betz limit in wind energy [15, 16]. These do not consider the interaction between the seawater environment and the extraction device.

1.4 Numerical methods

Shallow water equations are a set of hyperbolic partial differential equations that describe a fine layer of fluid with constant density in hydrostatic balance. Tides have a long period compared to the water depth, therefore they can be described by the shallow water system.
Shallow water equations are a complex system to be solved analytically. This led to considerable literature and software for numerical methods. The main methods to compute partial differential equations are:

- Finite Difference Method (FDM),
- Finite Element Method (FEM),
- Finite Volume Method (FVM).

All these methods imply the subdivision of the domain into a finite number of subdomains, elements or points. These methods have advantages and drawbacks, which are discussed below.

1.4.1 Finite Difference Method

The finite difference method is a differential scheme, which is an approximation of the Taylor series expansion. It gives a point-wise approximation to the partial differential equation. Then, it gives the result of dependent variables at discrete points.[37]

It is suitable for complex problems, it is a fast solver and the error can become negligible if it has a structured grid, hence the method becomes too rigid for irregular boundaries. [37]

The derivative of $q(x)$ is given by

$$u_x|_i = u_x(x_i) = \lim_{\Delta x \to 0} \frac{u(x_i + \Delta x) - u(x_i)}{\Delta x} \tag{1.1}$$

1.4.2 Finite Volume Method

The finite volume method can be used on all differential equations. It uses divergence operators to effectively write the equation. The next step is to do a volume integral of the equation. We can then apply Gauss's theorem. This converts the volume integral over the divergence into a surface integral over the boundaries. The integral thus changes from integrating the differential of the variable within the cells to surface integrals of the fluxes of the variable across the boundary of the cells. Suitable numerical approximation methods can usually be used to calculate these integrals. This leads to considerable simplification of the differential equation. This method is also suitable for unstructured grids and complex configurations. [33]

This is a strictly conservative method, however, in the case of a hyperbolic equation, it is not solved in a single algorithmic step, the conservative method of solving the equations may fail to provide the correct solution.[28]

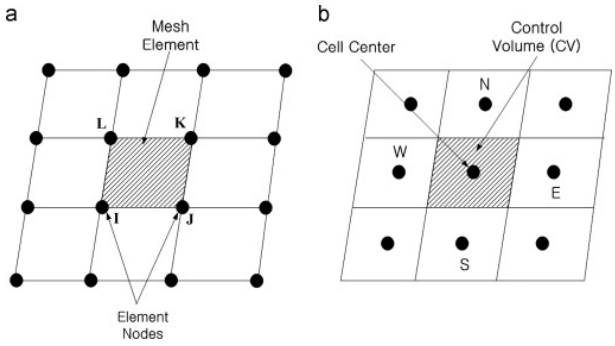

Figure 1.4: Finite element method and finite volume, grid examples.[21]

1.4.3 Finite Element Method

The finite element method is a general approach for elaborating approximate solutions to problems with boundaries. The FEM was originally developed for elliptical equations, but, it can be adapted to parabolic and hyperbolic problems.[28]

The main characteristics are the discretization of the domain, the approximation of the solution by a set of functions,

known as the shape functions or trial functions and the weak form of the governing equations. This emphasises the issue of multiple solutions, which is generally solved with the presence of only one solution with physical meaning. The system is solved through the integration form as the FVM. Thus the resolution of the system is easier to code even though can be more time-consuming for the machine.[37]

After the approximation of the solution, the fluxes are integrated by part to obtain the numerical fluxes on the edges. The grid is typically square or triangular in shape, like FVM, FEM is particularly suited for complex geometries, which offer a higher results accuracy. A problem with this method is the inability of dealing with discontinuity as a dam-break.

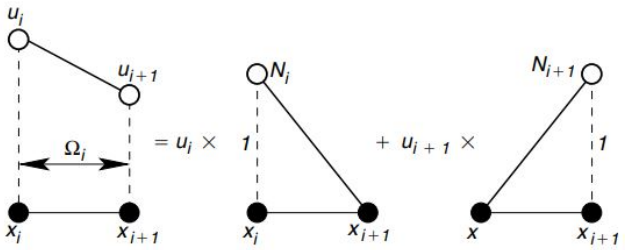

Figure 1.5: Finite element method, expansion bases. [31]

1.4.4 Discontinuous Galerkin method

In the end, the method selected to solve the swallow water system in this thesis is the discontinuous Galerkin method.

The discontinuous Galerkin method was introduced for the first time in 1973 by Reed and Hillis. It is a combination of the finite element and the finite volume. The Discontinuous Galerkin has features from both numerical methods, such as: the capability to model flows with significant horizontal velocity, direct implementation of boundary conditions through a numerical flux, suitability with unstructured grids to simulate complex geometries and offer higher accuracy within the flow field.

The discontinuous Galerkin allow a simple implementation of the fluxes between the elements by means of Riemann solvers and slope limiters. The method allows easy implementation of the TVD Runge-Kutta time integration scheme as each element is solved individually and one element is connected to the surrounding elements by boundary fluxes. Discontinuity can be easily resolved in the discontinuous Galerkin method because the nodes connecting the elements have two values.[28, 7] This method is strongly suitable for high-order formulation and scheme presenting discontinuity. On the other hand, it is high storage and high computational requirements.

1.5 Aims of the thesis

The assessment of tidal energy resources is essential to understand the local flow field around a tidal device and its evolution and interaction with the undisturbed fluid. It is also necessary to determine how the flow dynamics are affected by tidal devices and the amount of tidal energy resources available after extraction.

Following this idea, the aim of this thesis is to develop a tool to solve the shallow water equations using a numerical model based on the Finite Element Method. This code will allow the calculation of local current velocities. The

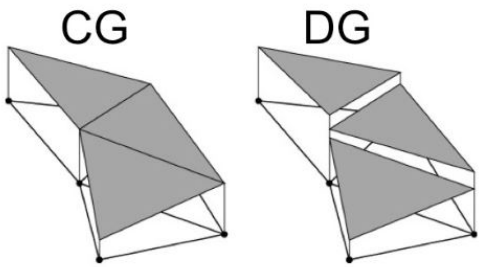

Figure 1.6: Continuous Galerkin (FEM) and Discontinuous Galerkin solution representation

shallow water equations describe the tidal hydrodynamics in coastal basins. This method can be accurately defined by the discontinuous finite element, in this case the discontinuous Galerkin method was chosen. Furthermore, this method allows the conservation of mass and momentum on an element basis, which guarantees a correct calculation of the flow rate, the momentum flux in the local field and the assessment of the tidal resources.

1.6 Thesis outline

This thesis includes a description of the discontinuous Galerkin method, development of the code to simulate the tidal local stream velocities and analysis of the error related to it.

Chapter 2 begins with a state of the art, followed by the tidal turbine classification and the projects deployed worldwide.

Chapter 3 presents the shallow water equations typically applied for the description and simulation of tidal hydrodynamics. Following this, Chapter 4 describes the numerical model implemented for the shallow water equations using the discontinuous Galerkin method in one-dimensional space and the Runge-Kutta technique for the time integration. Chapter 5 describes the numerical method implemented for the SWEs using the discontinuous Galerkin procedure in two-dimensional space and the Runge-Kutta technique for the time integration. Chapter 6 discusses the results from the one-dimensional code and analysed the associated error, and the results from the two-dimensional code.

Lastly, Chapter 7 presents the main conclusions and proposals for future work are made. In the appendix A a description of the case studied with the one-dimensional model. In appendices B and C there are more solutions and error representations of the one-dimensional case.

Chapter 2

Tidal stream turbine: state of the art

In the present chapter, a literature review of research and development of tidal stream turbine are presented. Earth-Moon system has lost mechanical energy and the Earth has slowed down due to tide movements, resulting in viscous dissipation in turbulence, at the seabed and in the coastal restriction, since the formation of this system. This loss of energy has been over millions of years, and the period of Earth's rotation increased from 21.9 to 24 hours in 620 million years. Even though tidal energy might collect more energy from this natural system, the effect will be negligible over humankind's existence. A tidal flow can be converted into electricity through a tidal generator, higher tidal current speed and wider tidal variation can significantly intensify the capability of a specific site. [2] Tidal streams with a fairly high speed are limited around the world since they need a concentrated natural tidal current flow. They can be found around the west and east coast of Canada, around the UK, especially Scotland, South Korea, Indonesia and north of Australia, as shown in figure 2.1.

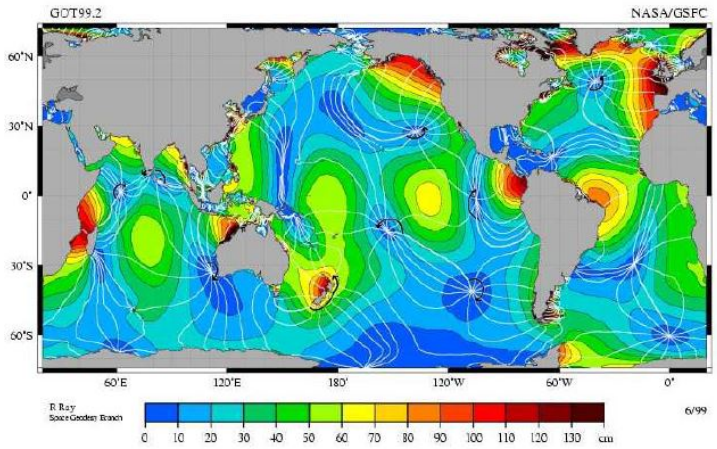

Figure 2.1: Geographical incident of the tidal range [52]

2.1 Tidal turbine classification

The European Marine Energy Centre classifies tidal stream turbines into four categories: axial-flow turbines, cross-flow axis turbines, oscillating devices and Venturi effect. They are described below and showed in figure 2.2, however other options are being studied [2, 8]:

- Horizontal axis turbines: they follow the same concept as wind turbines, which extract energy from moving air, while tidal horizontal axis turbines are crossed by water to produce energy.

- Cross-flow axis turbine: as previously mentioned their extraction of energy is similar to windmills, but their axis is perpendicular to the flow direction, and it can be mounted vertically or horizontally.

- Oscillating hydrofoil: these devices are attached to an arm and move up and down, where the hydrofoil sections are thrust sidewards by the flow instead of having rotational components.

- Enclosed tips (Venturi effect): they are equipped with a funnel-shaped shell, which concentrates the flow passing through the turbine, and the structure is completely submerged in the current. It can be installed vertically or horizontally.

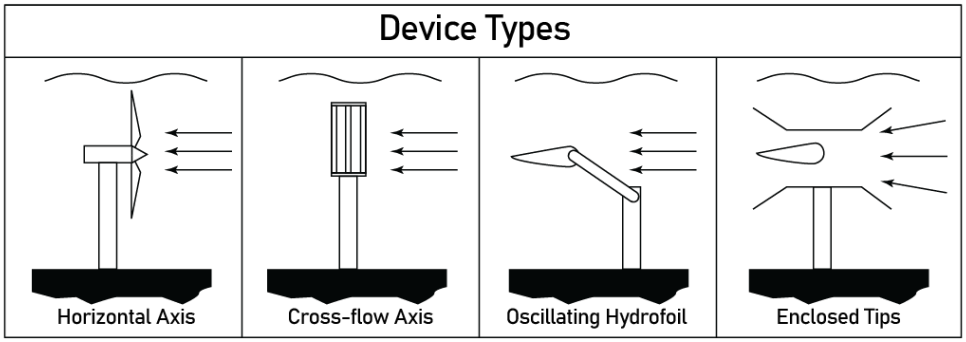

Figure 2.2: Tidal energy devices types.

EMEC recently added two new categories:

- Archimedes screw: it is a spiral-shaped device as shown in the figure 2.3, the turbine unsheathes the tidal stream power while the water flows up and through the helix rotating the turbine. It had been used as a pump since ancient times, and two centuries ago, it had been suggested as a reverse machine, alias a turbine. Even so, it has been studied as an option in the tidal stream field only in the last 20 years, without an actual complete project deployed.

- Tidal kite: it is tied up to the seabed by a tether and equipped with a turbine below the wings. It draws an eight-shape trajectory to increase the water velocity passing through the turbine. Indeed it is developed to low-speed current and the kite structure pushes the turbine to feel a speed faster than the actual flow rate.

Focusing on tidal turbine array layout can be distinguished between two generations. In the first generation, the minimisation of negative interaction effects among the devices and the maintenance logistic had a relevant weight on the final solution considered. The configuration, generally, had only two rows and the turbines are staggered in order to minimise the wake flow effect on the following row and have free access to each turbine from outside the array. Although, this scheme can lead to a very extended farm. The second generation is represented by research for the optimisation of the array, looking for a maximisation of the average power extraction, while limiting the wake effect on the following rows with the study of different scenarios. [27]

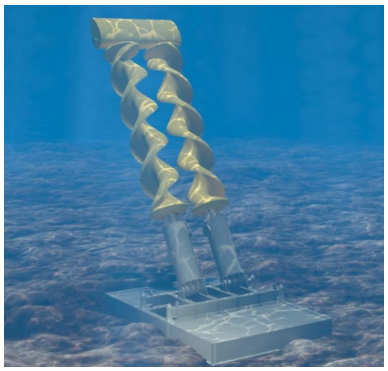

Figure 2.3: Archimedes screw turbine. [19]

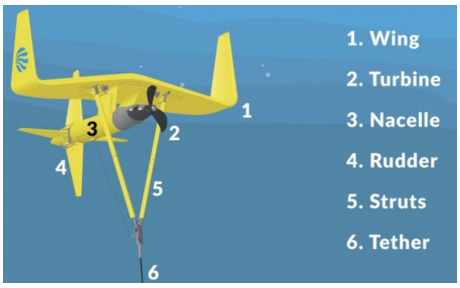

(a) Tidal kite

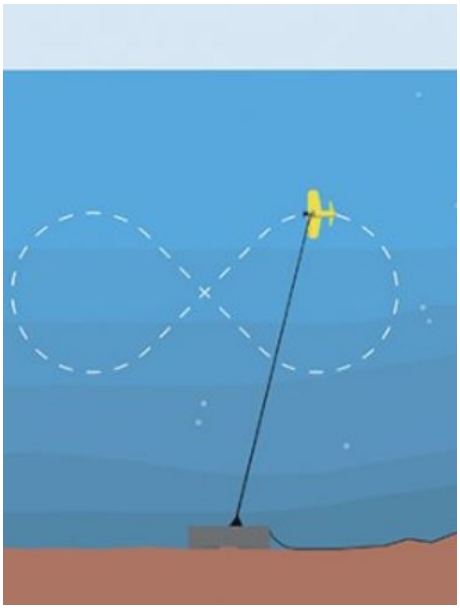

(b) Tidal kite path

Figure 2.4: Tidal kite and its path[25]

2.2 Projects deployed

The tidal current energy is improving, and the progress is proved by the operating hours, the electricity generated and the new capacity installed. The technologies are moving forward to the commercialization phase with the deployment of full-scale devices and arrays in actual sea conditions.

There were several test sites and prototypes installed, but not many of them have provided the results expected or proceeded with a full-scale prototype, the most interesting tests of tidal converters are:

- Kvalsund tidal turbine prototype: a 300kW turbine was deployed in Kvalsund (Norway) in 2003, the world's first tidal stream turbine to deliver electricity to the grid in 2004 and was operating until 2011. The prototype delivered over 1.5 GWh to the grid with the availability of 98% during the test period, showing the reliability and efficiency of the device. [43]

- Cormat: it is a 500kW contra-rotating turbine, deployed off the western coast of Mull of Kintyre (Scotland) in 2011, which test rapidly expanded to an array of 6 devices the following year. It uses two closely spaced

diverse rotors, turning in opposite directions. [29]

- Sabella D10: it is the first turbine entirely manufactured in France and deployed on the coast of Ushant Island (Brittany, France). The 1MW device has been operating since November 2015, it allowed monitoring of the marine environment and was perceived as a neutral impact. It will be replaced by an array of two devices in 2023.[36, 47, 13]

- LHD: the Chinese developer deployed four vertical-axis turbines in 2016 other two vertical-axis turbines and a horizontal-axis turbine in 2018. All turbines were in a range of power between 200 and 300kW, for a total amount of 1.7MW. The project was located near Xiushan Island (Zhejiang Province, China), and delivered to the grid a total of 1.95GWh until 2020. The project followed by adding a 1.6MW horizontal axis turbine at the beginning of 2022.[38, 50]

The tidal stream energy sector announced several projects under construction or in the development phase. There are only a few projects already supplying energy to the grid, which are presented below.

2.2.1 SeaGen Strangford Lough

SeaGen project was the first full-scale tidal energy project. It was composed of two Seagen S turbines of 600kW each, which were able to pitch through 180 degrees in order to higher efficiency in both directions of the flow. They were mounted on the same monopile with a crossbeam, which could be submerged to the desired depth and lifted out for maintenance. The project was commissioned at Strangford Lough in Northern Ireland in 2008 and delivered electricity to the grit until 2016, when Atlantis, the company owner of the project, announced the decommissioning of the device. Since the site supports important types of marine and coastal habitats with related species, the EIA report of this project represents a milestone for the sector and the demonstration of the low environmental impacts of tidal stream turbines. [41, 49]

2.2.2 Shetland tidal array

Shetland is a Scottish archipelago located among Orkney, Faroe Island and Norway, as shown in figure 2.5. This project was the first tidal stream energy array ever deployed worldwide. Nova Innovation installed it at Bluemull Sound in 2016. The project started with 3 turbines (Nova M100) of 100kW each. Since the positive response of those and more than 17,000 producing hours in 2019, Nova Innovation obtained the licences to extend the array to six turbines and increase the capacity up to 600kW. The fourth turbine was deployed in 2020, and the last two devices will be installed in 2022-2023. Furthermore, the company collaborated with Tesla for the installation of the first baseload tidal power plant, which is proving its ability to deliver constant power and meet the energy demand of the customers' needs. [45, 18]

Nova M100 is a bottom fixed turbine with a design of only two blades, which is more efficient in the water. On the other hand, it is more vulnerable to stress forces and the maximum tidal steam velocity supported is 2.6 m/s. [17]

Figure 2.5: Location of the tidal array deployed by Nova Innovation

2.2.3 MeyGen

The MeyGen project is located in the Inner Sound of Pentland Firth, between the Scottish mainland coast of Caithness and the uninhabited island of Stroma. This is a natural channel connecting the North Sea to the Atlantic Ocean where the water accelerates its passage. The MeyGen is the largest planned tidal stream array at the moment of writing and is currently the only commercial project under construction. [11] The project is divided into three main phases:

- Phase 1 - Operational: the first phase involves the deployment of four turbines of 1.5MW each. There are two types of turbine technologies (Atlantis Resources AR1500 and Andritz Hydro Hammerfest AH1000 MK1) mounted on gravity-base foundations, equipped with monitoring tools to observe and study the interaction between the marine life and the devices. [11] In September 2020, a subsea hub was installed, called Project Stormia. In order to allow the turbines to be connected to inter-array cable among them and have only one export cable, which will decrease the costs related to grid connection. This new hub will introduce two additional turbines for an amount of 4MW. [44]

- Phase 2 - in Development: it incorporates the installation of a supplementary 80MW of tidal stream power to the same site. It will be a milestone for the tidal energy sector and will prove the potential of the sector to the energy industry. [11]

- Phase 3 - in Development: MeyGen project has permission for tidal stream capacity up to 398MW when its grid is planned for 252MW, even though the site can support the whole 398MW permitted. [11]

The whole area has a potential available power of 1.9 GW. [12] The project delivered 13.8GWh to the grid in only 2019 and a tally of 43GWh from April 2018, the official start of the operational phase of the four turbines, until June 2022. [9]

2.2.4 Vestmannasund tidal power plant

Vestmannasund is Minesto's project location on Faroe Island. Minesto deployed the tidal kite of 100kW (Dragon 4) in the early summer of 2022. The first phase of power generation demonstrated the performance forecast with previous computational simulations. [24] They assert that the Deep Green technology is several hundred times more

productive than a stationary turbine since their turbine is actually ”flying” under the water with an eight-shaped trajectory and the wing propels the turbine through the flow. The relative velocity is higher than the actual current speed, which will increase electricity production. Moreover, it is the only technology able to operate at low speed in the cost-effective range. The minimum velocity proved is 1.2 m/s, which means it can use both tidal and ocean currents.[26]

2.2.5 From ScotRenewables SR2000 to O2: need to be revise

SR200 was the first floating tidal energy technology ever installed. The 2MW device was connected to the grid of Orkney Islands in November 2016, it is made of 2 turbines of 1MW each, both supported by a single floating structure, it was removed in September 2018 to make way for the updated version O2, which started generating power in July 2021, it is the most powerful tidal turbine in the present day with an estimated energy production of 5.19GWh. [35, 48]

2.2.6 U.S. and Canada projects

The U.S.A. has been tackling tidal streams since 2012, whereas Canada has been in the tidal energy sector since 1984 with Annapolis Royal tidal barrage power plant, in Nova Scotia. [5] The U.S.A presents two projects working nowadays:

- Roosevelt Island tidal energy project: it is a pilot project in New York, which is studying the East Channel of the East River within New York City and Manhattan borough with three Gen5 turbines deployed in October 2020. The research on the site started in 2002 with the RITE demonstration and continued with this project in 2012.[46] Verdant Power announced that the RITE project produced 100MWh in only 85 days of continuous operation, further more than what was projected. [10]

- Cobscook Bay project: it was developed by Ocean Renewable Power Company (ORPC) in Maine state. It delivered energy to the grid from September 2012 to July 2013 with only one device of 150kW. In the following years, mooring systems were tested and in 2022 a new turbine model will be deployed but it will not be connected to the grid. Even though it is a good site for testing, ORPC does not consider the location economically worth requiring the commercial license.[42] Connected to this second project, ORPC is planning 15 double TidGen hydrokinetic tidal devices of 500kW each, for a total of 5MW in Western Passage in Maine. [51]

Canada has two locations with some of the highest tidal ranges in the world, which are the Bay of Fundy, in Nova Scotia (Atlantic Ocean), and Ungava Bay, in British Columbia (Pacific Ocean). [5] Sustainable Marine Energy (SME) and Schottel Hydro are developing studies in the area of the Bay of Fundy. They connected to the grid PLAT-I 6.40 in 2021. This is a floating platform provided with six axial flow turbines of 70kW for a total amount of 420kW. The device was installed in Grand Passage and subsequently, it will move to Minas Passage, where the tides are more powerful. [30]

Chapter 3

Swallow water model

The shallow water equations have been used to describe the approximate progression of long waves in small water depths. This model can be derived from a control volume analysis of a fluid element with an infinitesimal two-dimensional area and the entire water depth. [22] To follow this analysis, some assumptions are necessary:

1. The flow is incompressible.
2. The free surface perturbation ζ is orders of magnitude smaller than the wavelength.
3. The diffusion of the momentum is negligible, which means the horizontal component of the hydrostatic gradient defines the flow direction.

The second assumption leads to two considerations, first, the streams are meanly horizontal, and second, the pressure in the vertical direction is approximately hydrostatic. While the third assumption implies that the weight is balanced by the hydrostatic pressure gradient, therefore, there is no vertical acceleration, which means the vertical velocity is uniform. Besides, the vertical velocity component is smaller than the horizontal components. Following these considerations, the vertical momentum flow rate is negligible as the free surface vertical movement since the vertical velocity is subjected to the mass balance. Therefore the piezometric pressure is vertically uniform, at the same time, the free surface perturbations generate horizontal balance disturbance of the piezometric pressure distribution. [22]

The depth must be at least three orders of magnitude smaller than the wavelength, otherwise, the model cannot be applied. This model can be applied to the actual shallow water of a few centimetres. However, it can determine the tidal hydrodynamics in coastal basins, considering the tidal waves are thousands of kilometres long and the sea depth reaches only a few kilometres.

The control volume is a cylinder with Γ as vertical walls, the seabed as the bottom boundary and the free surface as the upper boundary. The free surface perturbation at the boundary Γ is $\zeta(\theta, t)$, where θ is the linear coordinate of the boundary. The seabed bathymetry is represented by b(x,y).

The volume control analysis can be simplified to a two-dimensional system, where the velocity depends on time and horizontal coordinates. The domain is Ω and the boundary is Γ with $\mathbf{n}$ the outgoing normal as shown in figure 3.2.

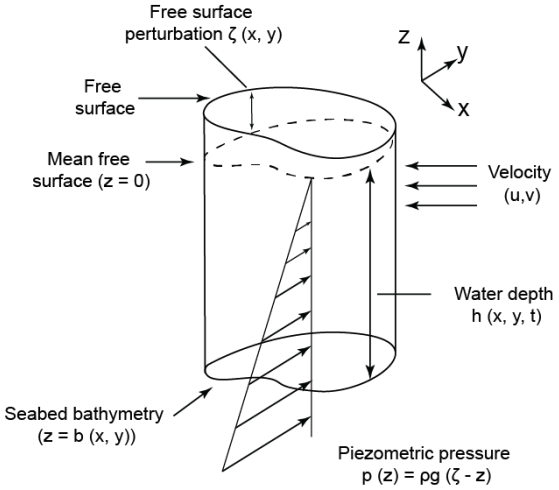

Figure 3.1: Shallow water model presented in a control volume, where the velocity have a larger horizontal component.

The conditions at the boundary are: the seabed is impermeable

$$(\mathbf{v} \cdot \mathbf{n})_b \;=\; 0 \tag{3.1}$$

and the free surface varies with the fluid

$$(\mathbf{v} \cdot \mathbf{n})_\zeta \;=\; 0 \tag{3.2}$$

After expressing the assumption and the boundary constraints, it is possible to focus on the mass conservation

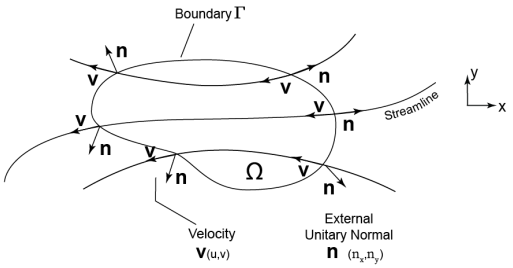

Figure 3.2: Top view of the control volume with the streamlines and the domain becomes Ω

equation on the control volume

$$\frac{d}{dt}\int_A \int_b^\zeta \rho dz dA \;+\; \int_\Gamma \int_b^\zeta \rho\,(\mathbf{v} \cdot \mathbf{n})\, dz d\Gamma \;=\; 0 \tag{3.3}$$

Moving to the two-dimensional system by integrating into z, since the velocity is vertically uniform. Furthermore, the equation can be divided by the density of the fluid and applied the Gauss theorem, to obtain

$$\frac{d}{dt}\int_A h dA \;+\; \int_\Gamma h\mathbf{v} \cdot \mathbf{n} d\Gamma \;=\; \int_A \left(\frac{\partial h}{\partial t} \;+\; \nabla \cdot (h\mathbf{v})\right) dA \;=\; 0 \tag{3.4}$$

In conclusion, the differential form of the conservation of the mass balance equation for the shallow water model

is

$$\lim_{A \to 0} \frac{1}{A} \int_A \left(\frac{\partial h}{\partial t} + \nabla \cdot (h\mathbf{v}) \right) dA = \frac{\partial h}{\partial t} + \nabla \cdot (h\mathbf{v}) = 0.$$

The momentum balance on the fixed control volume follows a similar procedure of the conservation of mass. Given the fact the piezometric pressure and the velocity are uniform in the depth coordinate, the balance is respected in a three-dimensional space as in a two-dimensional space. The local pressure is defined as $p(z) = \rho g(\zeta - z)$, where $h = (\zeta - z)$. It is important to remember that $z = 0$ is the mean free surface level, and below it, z is negative, while the free surface perturbation ζ can assume positive or negative values.

The momentum balance for the control volume is

$$\frac{d}{dt} \int_V \rho \mathbf{v} dV + \int_S \rho \mathbf{v} (\mathbf{v} \cdot \mathbf{n}) \, dS = - \int_S p \mathbf{n} dS \tag{3.5}$$

The integral of the pressure can be expressed in another form to simplify the calculation,

$$- \int_S p \mathbf{n} dS = - \int_A \int_b^\zeta \nabla p \, dz dA = - \int_A \int_b^\zeta \nabla \left(\rho g \left(\zeta - z \right) \right) dz dA = - \int_A \nabla \zeta \rho g h dA \tag{3.6}$$

and the momentum equation can be written as

$$\frac{d}{dt} \int_A \int_b^\zeta \rho \mathbf{v} dz dA + \int_\Gamma \int_b^\zeta \rho \mathbf{v} (\mathbf{v} \cdot \mathbf{n}) \, dz d\Gamma = - \int_A \nabla \zeta \rho g h dA \tag{3.7}$$

The flow is incompressible, as the assumption of the model, so the equation can be divided by the density ρ and integrated into z, resulting in

$$\frac{d}{dt} \int_A h \mathbf{v} dA + \int_\Gamma (h\mathbf{v} \otimes \mathbf{v}) \cdot \mathbf{n} d\Gamma = - \int_A \nabla \zeta g h dA. \tag{3.8}$$

Where the $\mathbf{v} \otimes \mathbf{v}$ indicates the matrix $\mathbf{v}\mathbf{v}^T$. [22] Applying the Gauss theorem to obtain

$$\frac{d}{dt} \int_A h \mathbf{v} dA + \int_A \nabla \cdot (h\mathbf{v} \otimes \mathbf{v}) \, dA = - \int_A \nabla \zeta g h dA \tag{3.9}$$

The infinitesimal dimension in the limit of a domain of the momentum equation is

$$\frac{\partial}{\partial t} (h\mathbf{v}) + \nabla \cdot (h\mathbf{v} \otimes \mathbf{v}) = gh \nabla \zeta. \tag{3.10}$$

Chapter 4

The Runge-Kutta Discontinuous Galerkin Method for one-dimensional shallow water equations

The shallow water equations can be presented in the conservative form as

$$\frac{\partial \mathbf{q}}{\partial t} + \frac{\partial \mathbf{F}}{\partial x} = \mathbf{s}, \tag{4.1}$$

with $x \in [0, L]$ and $t \in [0, \mathcal{T}]$. The $\mathbf{q}$ represents the vector of conservative variables, $\mathbf{F}$ is the flux vector and $\mathbf{s}$ describes the source term associated with the variation in the surface and the effect of fluid friction, are expressed by

$$\mathbf{q} = \begin{pmatrix} h \\ uh \end{pmatrix}, \quad \mathbf{F} = \begin{pmatrix} uh \\ hu^2 + \frac{1}{2}gh^2 \end{pmatrix}, \text{and} \quad \mathbf{s} = \begin{pmatrix} 0 \\ -gh\dfrac{db}{dx}. \end{pmatrix}. \tag{4.2}$$

The sea-bed bathymetry $b(x)$ is a given data. The system of equations 4.1 requires initial conditions $\mathbf{u}(x, 0)$, and boundary conditions $\mathbf{u}(0, t)$ and $\mathbf{u}(L, t)$ to be introduced later.[39]

The computational domain I is divided into a set of N elements I_e non-overlapping one another, with length Δx_e and defined as

$$I_e = \left[x_e - \frac{1}{2}\Delta x_e \, , \, x_e + \frac{1}{2}\Delta x_e \right] \tag{4.3}$$

where x_e is the middle point of the element. There are two types of boundaries: internal edges Γ^{int}, when the edge of the element is inside of the space I and external edges Γ^{bc}, which define the boundary conditions of the domain and interact with the ghost element. The edges and normals follow the same structure, in the subscript the first is related to the belonging element after the neighbour or ghost element, as presented in figure 4.1. The normals are pointing outward, from I_e to I_i is called $\hat{n}_{ei}$. Consequently, the opposite normal pointing from I_i toward I_e is called

$\hat{n}_{ie}$ and it has the inverse value of $\hat{n}_{ei}$, $\hat{n}_{ei} = -\hat{n}_{ie}$ and they assume the following values

$$\begin{aligned} \hat{n}_{ei} &= +1, \\ \hat{n}_{ie} &= -1. \end{aligned} \tag{4.4}$$

The external boundaries are defined through two ghost elements Ω_b^{bc}.

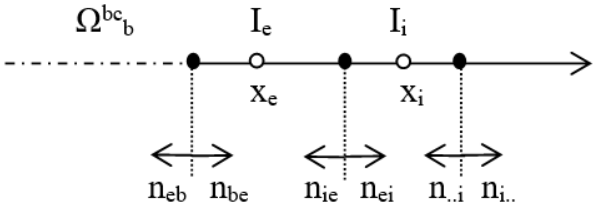

Figure 4.1: Definition of normals and edges of the elements I_e and the boundary condition

4.1 Weak formulation

The definition of the solution $\mathbf{q}$ needs an approximation $\mathbf{q}_h$ for a given time instant $t \in [0, T]$, which is classified into a finite dimensional space $W_h = W_h^k \equiv \{w : w\,|I_e \in P^k(I_e), 1 \leq e \leq N\}$, where $P^k(I_e)$ is the space of the polynomials in I_e of degree up to k, which weakens the formulation through the following steps.

First of all, $\mathbf{q}_h$ henceforward will be $\mathbf{q}$, dropping the subscript h for the sake of simplicity, although it remains a local solution to the element I_e.

The system of equations (4.1) is multiplied by a set of arbitrary smooth functions, called test functions $\phi(x)$, and then integrated into I_e.

$$\int_{I_e} \frac{\partial \mathbf{q}}{\partial t}\,\phi\,dx \;+\; \int_{I_e} \nabla \cdot \mathbf{F}\,\phi\,dx \;=\; \int_{I_e} \mathbf{s}\,\phi\,dx. \tag{4.5}$$

Afterwards, the flux is integrated by parts as

$$\int_{I_e} \frac{\partial \mathbf{q}}{\partial t}\phi dx \;-\; \int_{I_e} \mathbf{F}\,\frac{d\phi}{dx}dx \;+\; \Big(\mathbf{F}(q_{ei})\hat{n}_{ei}\phi\Big) \;+\; \Big(\mathbf{F}(q_{ej})\hat{n}_{ej}\phi\Big) \;=\; \int_{I_e} \mathbf{s}\,\phi dx. \tag{4.6}$$

Considering the discontinuity of the method, the fluxes on the edges are different, therefore they are substituted by the numerical fluxes $\mathbf{H}$, which depend on the two elements sharing the edge and the outward normal. [39]

$$\mathbf{H}_{ei} \;=\; \mathbf{H}\,(q_{ei},\, q_{ie},\, \hat{n}_{ei}) \tag{4.7}$$

The numerical flux needs to comply with the consistency condition

$$\mathbf{H}\,(q_{ei},\, q_{ie},\, \hat{n}_{ei}) \;=\; \mathbf{F}\,(q_{ei})\;\hat{n}_{ei} \tag{4.8}$$

and the direction stability condition

$$\mathbf{H}\left(q_{ei},\, q_{ie},\, \hat{n}_{ei}\right) \,=\, -\mathbf{H}\left(q_{ie},\, q_{ei},\, -\hat{n}_{ei}\right) \,=\, -\mathbf{H}\left(q_{ie},\, q_{ei},\, \hat{n}_{ie}\right). \tag{4.9}$$

4.2 The Roe flux function

The assessment of the eigenvalues and eigenvector of the flux in the shallow water model can be solved by the Roe flux function, which requires the equation 4.1 in a quasi-linear form

$$\frac{\partial \mathbf{q}}{\partial t} \,+\, \mathbf{A}\frac{\partial \mathbf{q}}{\partial x} \,=\, \mathbf{s} \tag{4.10}$$

$$\mathbf{A} \,=\, \frac{\partial \mathbf{F}}{\partial q} \,=\, \begin{pmatrix} 0 & 1 \\ gh - v^2 & 2v \end{pmatrix} \tag{4.11}$$

Using a similarity transformation, the matrix $\mathbf{A}$ can be decomposed as

$$\mathbf{A} \,=\, \mathbf{R}\mathbf{\Lambda}\mathbf{L} \tag{4.12}$$

where all the components are expressed as,

$$\mathbf{R} \,=\, \frac{1}{\sqrt{2c}} \begin{pmatrix} 1 & 1 \\ v + c & v - c \end{pmatrix} \tag{4.13}$$

$$\mathbf{\Lambda} \,=\, \begin{pmatrix} v + c & 0 \\ 0 & v - c \end{pmatrix} \tag{4.14}$$

$$\mathbf{L} \,=\, \frac{1}{\sqrt{2c}} \begin{pmatrix} -(v - c) & 1 \\ v + c & -1 \end{pmatrix}. \tag{4.15}$$

with $\mathbf{R}$ and $\mathbf{L}$ are the right and left set of eigenvectors, $\mathbf{\Lambda}$ is the set of eigenvalue and $c = \sqrt{gh}$ is the wave speed in shallow waters.

Given the states $\mathbf{q}_{ei}$ and $mathbf{q}_{ie}$ the Roe's flux function is presented as

$$\mathbf{H}_{ei} \,=\, \left(q_{ei},\, q_{ie},\, \hat{n}_{ei}\right) \,=\, \frac{1}{2}\left(\mathbf{F}_{ei}\mathbf{n_{ei}} \,+\, \mathbf{F}_{ie}\mathbf{n_{ie}} - |\mathbf{A}_m|((q_{ei} - q_{ie})\right) \tag{4.16}$$

when the matrix $\mathbf{A}_m$ is a function of the mean value of conservative value

$$q_{ei_m} \,=\, q_{ie_m} \,=\, \frac{1}{2}(q_{ei} + q_{ie}) \tag{4.17}$$

the same equation can be obtained in the opposite direction

$$\mathbf{H}_{ie} \,=\, \left(q_{ie},\, q_{ei},\, \hat{n}_{ie}\right) \,=\, \frac{1}{2}\left(\mathbf{F}_{ie}\mathbf{n_{ie}} \,+\, \mathbf{F}_{ei}\mathbf{n_{ei}} - |\mathbf{A}_m|((q_{ie} - q_{ei})\right) \tag{4.18}$$

concluding that

$$\mathbf{H}_{ei} = -\mathbf{H}_{ie} \tag{4.19}$$

4.3 Element transformation

The transformation to a master element is a convenient method for simplifying the computation. The master element is defined as $\hat{I} = [-1, 1]$ and ξ as local coordinate, as shown in figure 4.2. The transformation is determined as

$$\xi = \frac{2}{\Delta x_e}(x - x_e) \tag{4.20}$$

where Δx_e and x_e are, respectively, the length and the middle point of the element I_e

$$x_e = \frac{1}{2}(x_{e+1/2} + x_{e-1/2}). \tag{4.21}$$

When the reverse transformation is

$$x = x_e + \frac{\Delta x_e}{2}\xi \tag{4.22}$$

and the derivative of the inverse transformation is

$$\frac{dx}{d\xi} = \frac{\Delta x_e}{2}. \tag{4.23}$$

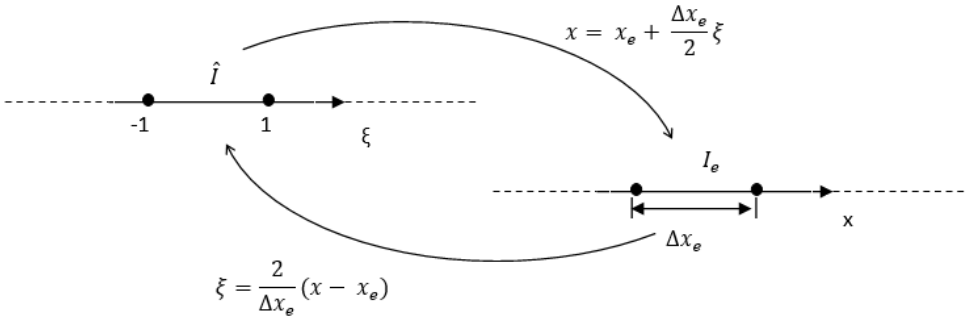

Figure 4.2: Transformation from element I_e to the standard element $\hat{I}$

The implementation of the element transformation 4.20 into the equation 4.6 as

$$\frac{\Delta x}{2}\int_{-1}^{1}\frac{\partial \mathbf{q}}{\partial t}\phi(\xi)d\xi - \int_{-1}^{1}\mathbf{F}\frac{d\phi}{d\xi}d\xi + \mathbf{H}_{ei}\,\phi_{ei} + \mathbf{H}_{ej}\,\phi_{ej} = \frac{\Delta x}{2}\int_{-1}^{1}\mathbf{s}\,\phi(\xi)d\xi. \tag{4.24}$$

4.4 Legendre polynomials and system of equation

The Legendre polynomial $p_m(\xi)$ is the option selected as a test function, thus the solution of k^{th}-order results in

$$q(\xi, t) = \sum_{m=0}^{k} p_m(\xi)\,\mathbf{q}_m(t) \tag{4.25}$$

where the m-order polynomial multiplies the conservative variables vector, presented as

$$\mathbf{q}_m \;=\; \begin{pmatrix} h_m \\ (hu)_m \end{pmatrix} \tag{4.26}$$

The Legendre polynomials are orthogonal over the defined interval $[-1\,,\,1]$, thus

$$\int_{-1}^{1} p_m(\xi)\, p_n(\xi)\, d\xi \;=\; \delta_{mn} \tag{4.27}$$

where the Kronecker delta is defined by

$$\delta_{mn} \;=\; \begin{cases} 1, & m \;=\; n \\ 0, & m \;\neq\; n \end{cases} \tag{4.28}$$

These polynomials are attainable using the subsequent recurrence equations

$$\begin{aligned}
p_0(\xi) &= 1\sqrt{\frac{2n+1}{2}} \;=\; \frac{\sqrt{2}}{2} \\
p_1(\xi) &= \sqrt{\frac{2n+1}{2}}\xi \;=\; \frac{\sqrt{6}}{2}\xi \\
p_2(\xi) &= \sqrt{\frac{2n+1}{2}}\,\frac{1}{2}\left(3\xi^2-1\right) \;=\; \frac{\sqrt{10}}{4}\left(3\xi^2-1\right) \\
p_3(\xi) &= \sqrt{\frac{2n+1}{2}}\,\frac{1}{2}\xi\left(5\xi^2-3\right) \;=\; \frac{\sqrt{14}\xi}{4}\left(5\xi^2-3\right) \\
p_4(\xi) &= \sqrt{\frac{2n+1}{2}}\,\frac{1}{8}\left(35\xi^4-30\xi^2+3\right) \;=\; \frac{3\sqrt{2}}{16}\left(35\xi^4-30\xi^2+3\right) \\
p_5(\xi) &= \sqrt{\frac{2n+1}{2}}\,\frac{1}{8}\xi\left(63\xi^4-70\xi^2+15\right) \;=\; \frac{\sqrt{22}\xi}{16}\left(63\xi^4-70\xi^2+15\right) \\
p_6(\xi) &= \sqrt{\frac{2n+1}{2}}\,\frac{1}{16}\left(231\xi^6-315\xi^4+105\xi^2-5\right) \;=\; \frac{\sqrt{26}}{32}\left(231\xi^6-315\xi^4+105\xi^2-5\right) \\
&\cdots \\
p_{n+1}(\xi) &= \frac{\sqrt{n+\frac{3}{2}}}{n+1}\Big(\,(2n+1)\,p_n\,\xi - n\,p_{n-1}\Big) \quad n=1,2,\cdots,k
\end{aligned} \tag{4.29}$$

At the boundary of the interval, the polynomials have the following formulae

$$\begin{aligned}
p_n(+1) \;&=\; \sqrt{\frac{2n+1}{2}} \\
p_n(-1) \;&=\; (-1)^n\sqrt{\frac{2n+1}{2}}.
\end{aligned} \tag{4.30}$$

The approximation of k^{th}-order of the solution occurs in $k-1$ variables $\mathbf{q}_n$ for each time instant. Implementing

the Legendre polynomial as smooth test function into 4.24, leads to

$$\frac{\Delta x}{2}\sum_{m=0}^{k}\frac{\partial \mathbf{q}_m(t)}{\partial t}\int_{-1}^{1} p_m p_n d\xi \;-\; \int_{-1}^{1}\mathbf{F}\,\frac{dp_n}{d\xi}d\xi \;+\; \mathbf{H}_{ei}\,p_n(-1) \;+\; \mathbf{H}_{ej}\,p_n(1) \;= \\ = \;\frac{\Delta x}{2}\int_{-1}^{1}\mathbf{s}\,p_n d\xi \tag{4.31}$$

with $n = 0, \cdots, k$. [39] And the Legendre orthonormality property obtains

$$\frac{\Delta x}{2}\frac{\partial \mathbf{q}_n}{\partial t} \;-\; \int_{-1}^{1}\mathbf{F}\,\frac{dp_n}{d\xi}d\xi \;+\; \mathbf{H}_{ei}\,p_n(-1) \;+\; \mathbf{H}_{ej}\,p_n(1) \;=\; \frac{\Delta x}{2}\int_{-1}^{1}\mathbf{s}\,p_n d\xi \tag{4.32}$$

This system of formulae for each segment I_e can be revised as

$$\frac{\partial \mathbf{q}_n}{\partial t} \;=\; \tilde{\mathbf{F}}_n \;-\; \tilde{\mathbf{H}}_n \;+\; \tilde{\mathbf{S}}_n \;=\; \boldsymbol{\mathcal{R}}_n(q) \tag{4.33}$$

where $\boldsymbol{\mathcal{R}}_n$ is defined as the residual, it will be used in the chapter 4.6, and the other vectors are described by

$$\tilde{\mathbf{F}}_n \;=\; \frac{2}{\Delta x}\int_{-1}^{1}\mathbf{F}(\mathbf{q})\,\frac{dp_n}{d\xi}d\xi; \tag{4.34}$$

$$\tilde{\mathbf{H}}_n \;=\; \frac{2}{\Delta x}\left(\mathbf{H}_{ei}p_n(-1) \;+\; \mathbf{H}_{ej}p_n(1)\right); \tag{4.35}$$

$$\tilde{\mathbf{S}}_n \;=\; \int_{-1}^{1}\mathbf{s}\,\phi_n d\xi \tag{4.36}$$

4.5 Integrals discretization

The integration is computed on the master element throughout the Gauss-Legendre quadrature rule with r points (ξ_b) and weights w_b, the method applied on the flux gives

$$\tilde{\mathbf{F}}_n \;=\; \sum_{b=1}^{g} w_b \mathbf{F}(q(\xi_b))\frac{\partial p_n(\xi_b)}{\partial \xi} \tag{4.37}$$

For polynomials with degrees up to $2r-1$, the Gauss-Legendre quadrature is accurate.[39] The same procedure is practised on the source term,

$$\tilde{S}_n \;=\; \sum_{b=1}^{g} w_b S(\xi_b) p_n(\xi_b) \tag{4.38}$$

4.6 Time integration

$\boldsymbol{\mathcal{R}}_n(q)$ is required for the discretization of the progression in time of the system of equations 4.33, an explicit third-order total variation diminishing (TVD) Runge-Kutta method has been used as follows:

$$\begin{aligned} q_n^{(1)} &= q_n^{(0)} + \Delta t \boldsymbol{\mathcal{R}}_n(q^{(0)}) \\ q_n^{(2)} &= \frac{3}{4} q_n^{(0)} + \frac{1}{4} q_n^{(1)} + \frac{1}{4} \Delta t \boldsymbol{\mathcal{R}}_n(q^{(1)}) \\ q_n^{(3)} &= \frac{1}{3} q_n^{(0)} + \frac{2}{3} q_n^{(2)} + \frac{2}{3} \Delta t \boldsymbol{\mathcal{R}}_n(q^{(2)}) \end{aligned} \tag{4.39}$$

where superscript numbers are the progression in time and zero refers to the initial condition imposed.[39] Stable condition is verified by

$$\Delta t \leq \frac{\Delta x_{min}\, f_1}{\lambda_{max}}\, CFL \tag{4.40}$$

with Δx_{min} is shortest segment I_e in the physical space, CFL is Courant-Friedrichs-Lewy number which is defined between 0 and 1, and λ_{max} and f_1 are given by

$$\lambda_{max} = |v| + c \tag{4.41}$$

$$f_1 = (2k+1)^{-1} \tag{4.42}$$

4.7 Boundary conditions

There are two boundary conditions to consider: the inlet flow and the outlet depth.
The inlet boundary related to the flow rate at the interface between I_e and Ω_b^{bc} is established by the ghost cell state

$$q_{be}^{bc,in} = \begin{pmatrix} h_{be} \\ q_{be} \end{pmatrix} = \begin{pmatrix} h_{eb} \\ (hu)_{in} \end{pmatrix} \tag{4.43}$$

While the depth is defined for the ghost cell by the inner element. The numerical flux boundary is given by

$$H_{eb} = H(q_{eb}, q_{be}^{bc,in}, \hat{n}_{eb}). \tag{4.44}$$

The outlet boundary related to the water depth at the interface between I_e and Ω_b^{bc} is a state defined on the ghost cell as

$$q_{be}^{bc,ou} = \begin{pmatrix} h_{be} \\ q_{be} \end{pmatrix} = \begin{pmatrix} h_{ou} \\ (hu)_{eb} \end{pmatrix} \tag{4.45}$$

The flow rate is defined by the inner element, therefore $q_{ou} = q_{eb} = q_{be}$.The numerical flux boundary is given by

$$H_{eb} = H(q_{eb}, q_{be}^{bc,ou}, \hat{n}_{eb}). \tag{4.46}$$

4.8 Computational implementation

For this code, it has been chosen the application of matrices product and matrix-vector product, since they are less computationally time-consuming than the for-loop cycles. This time saved can be considered pointless in a one-dimensional model, but it will be relevant for the two-dimensional implementation.
This section is divided into elementwise, edgewise and time integration.

4.8.1 Element integration

The solution presented in equation 4.25 can be reformulated, taking into consideration the Gauss-Legendre point, in a matrix form as

$$\mathbf{q}(\xi,t) \;=\; \sum_{m=0}^{k}\sum_{l=1}^{r} p_m(\xi_b)\,\mathbf{q}_m(t) \;=\; (\mathbf{P}(\xi))^T\,\hat{q}(t) \tag{4.47}$$

with $0 < m < k$ and $1 < l < r$, which determined the matrix of the Legendre polynomials $\mathbf{P}(\xi)$ and conservative variables matrix $\hat{q}(t)$

$$\mathbf{P}(\xi) \;=\; \begin{pmatrix} p_0(\xi_1) & p_0(\xi_2) & \dots & p_0(\xi_g) \\ p_1(\xi_1) & p_1(\xi_2) & \dots & p_1(\xi_g) \\ \dots & \dots & \dots & \dots \\ p_d(\xi_1) & p_d(\xi_2) & \dots & p_d(\xi_g) \end{pmatrix} \tag{4.48}$$

$$\hat{q}(t) \;=\; \begin{pmatrix} h_0 & (hu)_0 \\ h_1 & (hu)_1 \\ \dots & \dots \\ h_d & (hu)_d \end{pmatrix} \;=\; \begin{pmatrix} \mathbf{q}_0^T \\ \mathbf{q}_1^T \\ \dots \\ \mathbf{q}_d^T \end{pmatrix} \tag{4.49}$$

The flux equation 4.37 in a matrix form is given by

$$\tilde{F} \;=\; \frac{2}{\Delta x}\,\frac{dP}{d\xi}\,(W \odot F) \tag{4.50}$$

where

$$\frac{\mathbf{P}}{dx} \;=\; \begin{pmatrix} \frac{\partial p_0}{\partial \xi}(\xi_1) & \frac{\partial p_0}{\partial \xi}(\xi_2) & \dots & \frac{\partial p_0}{\partial \xi}(\xi_g) \\ \frac{\partial p_1}{\partial \xi}(\xi_1) & \frac{\partial p_1}{\partial \xi}(\xi_2) & \dots & \frac{\partial p_1}{\partial \xi}(\xi_g) \\ \dots & \dots & \dots & \dots \\ \frac{\partial p_d}{\partial \xi}(\xi_1) & \frac{\partial p_d}{\partial \xi}(\xi_2) & \dots & \frac{\partial p_d}{\partial \xi}(\xi_g) \end{pmatrix}, \tag{4.51}$$

$$W \;=\; \begin{pmatrix} w_1 \\ w_2 \\ \dots \\ w_g \end{pmatrix}, \tag{4.52}$$

$$F = \begin{pmatrix} F^T(\mathbf{q}_1) \\ F^T(\mathbf{q}_2) \\ ... \\ F^T(\mathbf{q}_g) \end{pmatrix} \tag{4.53}$$

It is important to notice that $\odot$ is a symmetric product, so it is a linear product between the elements of the vector and the matrix.

Following the same procedure, the source terms are defined as

$$\tilde{s} = \mathbf{P}\,(W \odot S) \tag{4.54}$$

with

$$S = \begin{pmatrix} s^T(\mathbf{q}_1) \\ s^T(\mathbf{q}_2) \\ ... \\ s^T(\mathbf{q}_g) \end{pmatrix} \tag{4.55}$$

4.8.2 Edge integration

The edges are presented by two points: ± 1; the conservative variables $\mathbf{q}$ need to be computed at the two edges, as follows

$$\mathbf{q}^{ed}(\xi, t) = (\mathbf{P}^{ed})^T\,\hat{q}(t) \tag{4.56}$$

where $\mathbf{P}^{ed}$ indicates that the calculations are related to the edges of the master element.

Therefore the numerical fluxes are given by

$$\tilde{H} = \frac{2}{\Delta x}\,\mathbf{P}^{ed} H \tag{4.57}$$

with

$$\mathbf{P}^{ed} = \begin{pmatrix} p_0(-1) & p_0(+1) \\ p_1(-1) & p_1(+1) \\ ... & ... \\ p_k(-1) & p_k(+1) \end{pmatrix}, \tag{4.58}$$

and

$$H = \begin{pmatrix} H_{ej}^T(\mathbf{q}_1) \\ H_{ei}^T(\mathbf{q}_2) \end{pmatrix}. \tag{4.59}$$

The only matrix equal all along the computation is $\hat{q}(t)$ because it depends only on time.

4.8.3 Time integration

The Runge-Kutta method for the time discretization presented in the set of equations 4.39 is determined by

$$\begin{aligned}
\hat{q}^{(1)} &= \hat{q}^{(0)} + \Delta t\, \boldsymbol{\mathcal{R}}(\hat{q}^{(0)}) \\
\hat{q}^{(2)} &= \frac{3}{4}\hat{q}^{(0)} + \frac{1}{4}\hat{q}^{(1)} + \frac{1}{4}\Delta t\, \boldsymbol{\mathcal{R}}(\hat{q}^{(1)}) \\
\hat{q}^{(3)} &= \frac{1}{3}\hat{q}^{(0)} + \frac{2}{3}\hat{q}^{(2)} + \frac{2}{3}\Delta t\, \boldsymbol{\mathcal{R}}(\hat{q}^{(2)})
\end{aligned} \tag{4.60}$$

with

$$\boldsymbol{\mathcal{R}} = \tilde{F} - \tilde{H} + \tilde{s} \tag{4.61}$$

These equations are calculated for each element.

4.9 Error evaluation

The numerical solution has three components of the error: the discretization error, the round-off error and the iterative error. [34]

The iterative error occurs due to the non-linear system of the differential equations. When it reaches the minimum, the solution converges, but it is never zero. The minimum is related to the size of the round-off error, which depends on the precision of the machine. In this case, the error corresponds to the residual. While the discretization error is linked to the polynomial functions made for the system of ordinary differential equations. It is a function of the polynomial's order g and the size of the mesh b. Let's consider q_i the numerical solution of the specific state i. The L_2 norm for the discretization error is given by

$$L_2 = \sqrt{\frac{1}{L}\int_0^L (q_i - q_{an})^2\, dx} = \alpha b_i^g + H.O.T. \tag{4.62}$$

with L the total area of the mesh, δ_{an} is the exact analytical solution and α is the the leading error term coefficient. If the mesh size is refined enough to achieve the asymptotic range, all higher-order terms (H.O.T.) become irrelevant, and g becomes the element defining the order of accuracy. [34]

The order of accuracy can be computed from the slope of a straight line defined by the discretization error linear regression, in a double-logarithmic scale

$$ln(L_2) = (g+1)ln(b_i) + lin(\alpha). \tag{4.63}$$

Chapter 5

The Runge-Kutta Discontinuous Galerkin Method for two-dimensional shallow water equations

The shallow water equations in 2D are obtained considering the second velocity component in the vertical direction and a second equation for the momentum, this leads to a system of three equations:

$$\frac{\partial h}{\partial t} + \frac{\partial hu}{\partial x} + \frac{\partial hv}{\partial y} = 0 \tag{5.1}$$

$$\frac{\partial hu}{\partial t} + \frac{\partial hu^2}{\partial x} + \frac{\partial huv}{\partial y} = -gh\frac{\partial b}{\partial x} \tag{5.2}$$

$$\frac{\partial hv}{\partial t} + \frac{\partial huv}{\partial x} + \frac{\partial hv^2}{\partial y} = -gh\frac{\partial b}{\partial y} \tag{5.3}$$

with $x \in [0, L]$, $y \in [0, D]$ in the space Ω and $t \in [0, \mathcal{T}]$. Following the previous nomenclature, $\mathbf{q}$ is the vector of conservative variables, $\mathbf{F}$ the flux vector, and $\mathbf{s}$ the source term, the equations can be presented in the conservative form

$$\frac{\partial \mathbf{q}}{\partial t} + \nabla \mathbf{F}(\mathbf{q}) = \mathbf{s}, \tag{5.4}$$

and each variable is a vector

$$\mathbf{q} = \begin{pmatrix} h \\ uh \\ vh \end{pmatrix}, \quad \mathbf{F} = \begin{pmatrix} uh & vh \\ hu^2 + \frac{1}{2}gh^2 & uvh \\ uvh & hv^2 + \frac{1}{2}gh^2 \end{pmatrix}, \quad \text{and} \quad \mathbf{s} = \begin{pmatrix} 0 \\ -gh\dfrac{db}{dx} \\ -gh\dfrac{db}{dy} \end{pmatrix}. \tag{5.5}$$

The sea-bed bathymetry $b(x)$ is a given data. The system of equations (5.4) requires an appropriate initial conditions $\mathbf{q}(x, y, 0)$, and boundary conditions $\mathbf{q}(\partial\Omega, t)$ to be introduced later. The computational domain Ω is subdivided into a set of N elements Ω_e of a triangular shape and non-superimposed one another. The boundary conditions are

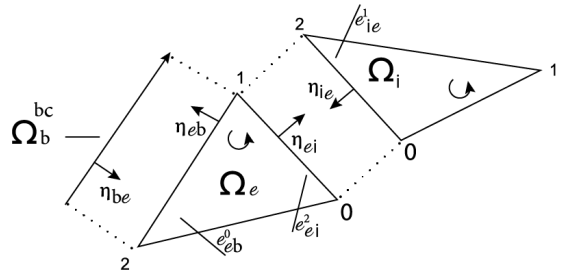

Figure 5.1: Representation of the tangents and the normals on the global space from element Ω_e and the connection with the boundary and the neighbour element Ω_j

introduced by designing ghost elements Ω_b^{bc} constituted by only one edge e_b^{bc}. The elements' boundaries are divided into two sets, internal edges Γ^{int} when the edge of the element is inside of the space Ω, and external edges Γ^{bc}, which define the boundary conditions of the domain and interact with the ghost elements. The nodes and edges go from 0 to 2 counterclockwise and the edge has the number of the opposite node. Therefore, each edge presents three indexes: in the superscript, the number relates to the position in the master element, in the subscript, first the belonging element after the neighbour or ghost element, as presented in figure 5.1.

In addition, the normals of the edges have different indexing, the normal of an edge of the internal set pointing from Ω_e to Ω_j is called $\hat{n}_{ei}$, consequently, the opposite normal pointing from Ω_j toward Ω_e is called $\hat{n}_{ie}$ and it has the inverse value of $\hat{n}_{ei}$, $\hat{n}_{ei} = -\hat{n}_{ie}$.[39]

5.1 Weak formulation

The system of equation is multiplied with a set of arbitrary smooth called test functions $\phi \in \Re^2$, followed by the integration over an element Ω_e.

$$\int_{\Omega_e} \frac{\partial q}{\partial t}\,\phi d\Omega + \int_{\Omega_e} \nabla \mathbf{F}\,\phi d\Omega = \int_{\Omega_e} \mathbf{s}\,\phi d\Omega \tag{5.6}$$

Afterwards, the flux is integrated by part

$$\int_{\Omega_e} \frac{\partial q}{\partial t}\,\phi d\Omega + \int_{\Omega_e} \mathbf{F}\cdot\nabla\phi d\Omega + \int_{\Gamma_e} \mathbf{F}\cdot\mathbf{n}\phi d\Gamma = \int_{\Omega_e} \mathbf{s}\,\phi d\Omega \tag{5.7}$$

Where Γ_e are the edges of the element Ω_e. Following the element boundaries previously described, the edges' flux has to be divided into internal and boundary condition

$$\int_{\Omega_e} \frac{\partial \mathbf{q}}{\partial t}\,\phi d\Omega + \int_{\Omega_e} \mathbf{F}\cdot\nabla\phi d\Omega + \sum_{\Gamma_e^{int}} \int_{e_{ei}} \mathbf{F}(\mathbf{q}_{ei})\cdot\mathbf{n}_{ei}\phi d\Gamma + \sum_{\Gamma_e^{bc}} \int_{e_{eb}} \mathbf{F}(\mathbf{q}_{eb})\cdot\mathbf{n}_{eb}\phi d\Gamma = \int_{\Omega_e} \mathbf{s}\,\phi d\Omega \tag{5.8}$$

Considering the discontinuous nature of the method, the flux terms on the edges are not unique, therefore the fluxes are substituted by a numerical flux $\mathbf{H}$,[39] and get

$$\begin{aligned}\int_{\Omega_e} \frac{\partial \mathbf{q}}{\partial t}\,\phi d\Omega + \int_{\Omega_e} \mathbf{F}(\mathbf{q})\cdot\nabla\phi d\Omega + \sum_{\Gamma_e^{int}}\int_{e_{ei}} \mathbf{H}(\mathbf{q}_{ei};\mathbf{q}_{ie};\mathbf{n}_{ei})\phi d\Gamma \\ + \sum_{\Gamma_e^{bc}}\int_{e_{eb}} \mathbf{H}(\mathbf{q}_{eb};\mathbf{q}_b^{bc};\mathbf{n}_{eb})\phi d\Gamma = \int_{\Omega_e}\mathbf{s}\,\phi d\Omega\end{aligned} \tag{5.9}$$

5.2 The Lax-Friedrichs flux

The eigenvectors and eigenvalues for the two-dimensional shallow water system need the quasi-linear form to be computed

$$\frac{\partial \mathbf{q}}{\partial t} + \frac{\partial \mathbf{F}_x}{\partial \mathbf{q}}\frac{\partial \mathbf{q}}{\partial x} + \frac{\partial \mathbf{F}_y}{\partial \mathbf{q}}\frac{\partial \mathbf{q}}{\partial y} = \frac{\partial \mathbf{q}}{\partial t} + \mathbf{A}\frac{\partial \mathbf{q}}{\partial x} + \mathbf{B}\frac{\partial \mathbf{q}}{\partial y} = s \tag{5.10}$$

with

$$\mathbf{A} = \begin{pmatrix} 0 & 1 & 0 \\ c^2-u^2 & 2u & 0 \\ -uv & v & u \end{pmatrix} \qquad \mathbf{B} = \begin{pmatrix} 0 & 0 & 1 \\ -uv & v & u \\ c^2-v^2 & 0 & 2v \end{pmatrix} \tag{5.11}$$

The two matrices can be combined in the characteristic matrix defined as

$$\mathbf{K} = \mathbf{A}n_x + \mathbf{B}n_y = \begin{pmatrix} 0 & n_x & n_y \\ c^2 n_x - u\mathbf{v}\cdot\mathbf{n} & un_x + \mathbf{v}\cdot\mathbf{n} & un_y \\ -v\mathbf{v}\cdot\mathbf{n} + c^2 n_y & vn_x & vn_y + \mathbf{v}\cdot\mathbf{n} \end{pmatrix} \tag{5.12}$$

Using a similarity transformation, the matrix $\mathbf{K}$ can be decomposed as

$$\mathbf{K} = \mathbf{R}\mathbf{\Lambda}\mathbf{L} \tag{5.13}$$

where the component care expressed by

$$\mathbf{\Lambda} = \begin{pmatrix} \mathbf{v}\cdot\mathbf{n}+c & 0 & 0 \\ 0 & \mathbf{v}\cdot\mathbf{n} & 0 \\ 0 & 0 & \mathbf{v}\cdot\mathbf{n}-c \end{pmatrix} \tag{5.14}$$

$$\mathbf{R} = \begin{pmatrix} 1 & 0 & 1 \\ u + cn_x & -n_y & u - cn_x \\ v + cn_y & n_x & v - cn_y \end{pmatrix} \tag{5.15}$$

and

$$\mathbf{L} = \begin{pmatrix} c - \mathbf{v}\cdot\mathbf{n} & n_x & n_y \\ 2c(un_y - vn_x) & -2cn_y & 2cn_x \\ c + \mathbf{v}\cdot\mathbf{n} & -n_x & -n_y \end{pmatrix} \tag{5.16}$$

The numerical flux functions have the same structure as the one-dimensional case, therefore the Lax-Friedrichs

flux is given by

$$\mathbf{H}(\mathbf{q}_{ei},\, \mathbf{q}_{ie},\, \mathbf{n}_{ei}) \;=\; \frac{1}{2}\Big(\mathbf{F}(\mathbf{q}_{ei}) \,\cdot\, \mathbf{n}_{ei} \;+\; \mathbf{F}(\mathbf{q}_{ie}) \,\cdot\, \mathbf{n}_{ie} \;-\; \lambda_{max}(\mathbf{q}_{ie} - \mathbf{q}_{ei})\Big) \tag{5.17}$$

The maximum eigenvalue is computed using

$$\lambda_{max} \;=\; max\,(\lambda_{max}(\mathbf{q}_{ei}),\, \lambda_{max}(\mathbf{q}_{ie})) \tag{5.18}$$

with $\lambda_{max} \;=\; |\mathbf{v} \cdot \mathbf{n}| + c$.[39]

5.3 Element transformation

An element transformation is a powerful tool for implementing the two-dimensional problem with the finite-element method. While in the one-dimensional problem, this transformation was trivial, the two-dimension has a few steps. The element transformation is also useful at the computational level. Instead, have only one gigantic matrix with sparse values, there is a set of matrices for each element e of the mesh with $1 < e < N$, where each element Ω_e is the image of the fixed standard element $\hat{\Omega}$ with a sequence of transformations $T_1, T_2, ..., T_N$ of the form

$$T_e : \begin{cases} x = x(\xi, \eta) \\ y = y(\xi, \eta) \end{cases} \tag{5.19}$$

where the transformation T_e is the map of $\hat{\Omega}$ on Ω_e.

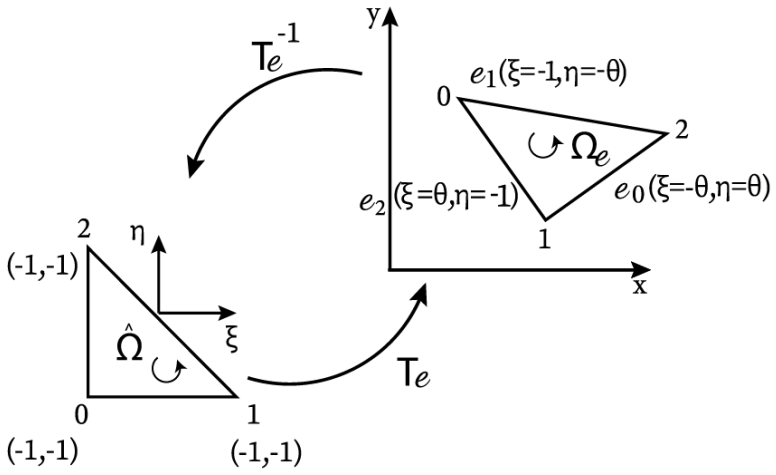

Figure 5.2: Transformation from element Ω_e to $\hat{\Omega}$ through T_e map

Let consider that the functions derivation of x and y respect to ξ and η are continuous, then the infinitesimal transformation $d\xi\ d\eta$ in dx and dy are

$$dx = \frac{\partial x}{\partial \xi} d\xi + \frac{\partial x}{\partial \eta} d\eta \quad \text{and} \quad dy = \frac{\partial y}{\partial \xi} d\xi + \frac{\partial y}{\partial \eta} d\eta \tag{5.20}$$

They can be written in the form of a matrix, where the matrix of the partial derivatives is named Jacobian matrix

of transformation.

$$\mathbf{J} = \begin{bmatrix} \frac{\partial x}{\partial \xi} & \frac{\partial x}{\partial \eta} \\ \frac{\partial y}{\partial \xi} & \frac{\partial y}{\partial \eta} \end{bmatrix} \tag{5.21}$$

$$\begin{bmatrix} dx \\ dy \end{bmatrix} = \mathbf{J} \begin{bmatrix} d\xi \\ d\eta \end{bmatrix} \tag{5.22}$$

The inverse map T_e^{-1} as the transformation from $x - y$ coordinates into $\xi - \eta$ coordinates can be obtained with the inverse of the Jacobian. The matrix to be invertible, the determinant need to be different from zero.

$$det\mathbf{J} = \frac{\partial x}{\partial \xi}\frac{\partial y}{\partial \eta} - \frac{\partial x}{\partial \eta}\frac{\partial y}{\partial \xi} \neq 0 \tag{5.23}$$

Therefore the inverse system transformation

$$T_e^{-1} : \begin{cases} \xi = \xi(x, y) \\ \eta = \eta(x, y) \end{cases} \tag{5.24}$$

can be written as

$$\begin{bmatrix} d\xi \\ d\eta \end{bmatrix} = \begin{bmatrix} \frac{\partial y}{\partial \eta} & -\frac{\partial x}{\partial \eta} \\ -\frac{\partial y}{\partial \xi} & \frac{\partial x}{\partial \xi} \end{bmatrix} \begin{bmatrix} dx \\ dy \end{bmatrix}. \tag{5.25}$$

Considering the local basis functions of the finite elements to construct T_e transformation,

$$T_e : \begin{cases} x = \sum_{p=1}^{M} x_i \psi_i(\xi, \eta) \\ \\ y = \sum_{p=1}^{M} y_i \psi_i(\xi, \eta) \end{cases} \tag{5.26}$$

M represents the number of nodes in the element. The element shape functions $\psi^e(x, y)$ for the element Ω_e are built from $\psi_p(\xi, \eta)$

$$\psi^e(x, y) \ = \psi_p(\xi(x, y), \eta(x, y)) \tag{5.27}$$

The elements are triangular, therefore the function $\mathbf{q}$ is represented by three local basis functions ψ_i.

$$\mathbf{q}^e = q_1\psi_1(\xi, \eta) + q_2\psi_2(\xi, \eta) + q_3\psi_3(\xi, \eta) \tag{5.28}$$

Assuming a linear triangular element in the physical space, the local basis functions are linear in the master element and they are given by

$$\psi_0 = -\frac{1}{2}(\xi + \eta) \qquad \psi_1 = \frac{1}{2}(\xi + 1) \qquad \psi_2 = \frac{1}{2}(\eta + 1) \tag{5.29}$$

The derivatives or the basis functions follow the chain rule

$$\frac{\partial \boldsymbol{\psi}^e}{\partial x} = \frac{\partial \boldsymbol{\psi}^e}{\partial \xi}\frac{\partial \xi}{\partial x} + \frac{\partial \boldsymbol{\psi}^e}{\partial \eta}\frac{\partial \eta}{\partial x} \qquad \frac{\partial \boldsymbol{\psi}^e}{\partial y} = \frac{\partial \boldsymbol{\psi}^e}{\partial \xi}\frac{\partial \xi}{\partial y} + \frac{\partial \boldsymbol{\psi}^e}{\partial \eta}\frac{\partial \eta}{\partial y} \tag{5.30}$$

Assessing the derivatives of 5.26 as presented in 5.20 it is possible to conclude

$$\frac{\partial x}{\partial \xi} = x_e \cdot \frac{\partial}{\partial \xi}\boldsymbol{\psi}^e(\xi,\eta) \tag{5.31}$$
$$\frac{\partial x}{\partial \eta} = x_e \cdot \frac{\partial}{\partial \eta}\boldsymbol{\psi}^e(\xi,\eta) \tag{5.32}$$
$$\frac{\partial y}{\partial \xi} = y_e \cdot \frac{\partial}{\partial \xi}\boldsymbol{\psi}^e(\xi,\eta) \tag{5.33}$$
$$\frac{\partial y}{\partial \eta} = y_e \cdot \frac{\partial}{\partial \eta}\boldsymbol{\psi}^e(\xi,\eta) \tag{5.34}$$
$$\tag{5.35}$$

Therefore the relation between the differentials is defined as

$$\begin{bmatrix} \frac{\partial \xi}{\partial x} & \frac{\partial \xi}{\partial y} \\ \frac{\partial \eta}{\partial x} & \frac{\partial \eta}{\partial y} \end{bmatrix} = \frac{1}{det\mathbf{J}(\xi,\eta)} \begin{bmatrix} \frac{\partial y}{\partial \eta} & -\frac{\partial x}{\partial \eta} \\ -\frac{\partial y}{\partial \xi} & \frac{\partial x}{\partial \xi} \end{bmatrix} = \frac{1}{det\mathbf{J}(\xi,\eta)} \begin{bmatrix} \mathbf{y}\frac{\partial}{\partial \eta}\boldsymbol{\psi}^e(\xi,\eta) & -\mathbf{x}\frac{\partial x}{\partial \eta}\boldsymbol{\psi}^e(\xi,\eta) \\ -\mathbf{y}\frac{\partial y}{\partial \xi}\boldsymbol{\psi}^e(\xi,\eta) & \mathbf{x}\frac{\partial x}{\partial \xi}\boldsymbol{\psi}^e(\xi,\eta) \end{bmatrix} \tag{5.36}$$

whence it is possible to compute the transformation 5.26.

The final step is the transformation of the function $\mathbf{q}$ of x and y in the element Ω_e into $\mathbf{q}$ of ξ and η in the reference element $\hat{\Omega}$.

$$\mathbf{q}(x,y) = \mathbf{q}(x(\xi,\eta), y(\xi,\eta)) = \mathbf{q}(\xi,\eta) \tag{5.37}$$

where $x(\xi,\eta)$ and $y(\xi,\eta)$ are shown in the transformation T_e, equation 5.19.
Following the integration requirement of the shallow water system, the transformation of volume integral to the local space is the equation 5.38

$$\int_{\Omega_e} \mathbf{q}(x,y)dxdy = \int_{\hat{\Omega}} \mathbf{q}(\xi,\eta)\ det\mathbf{J}(\xi,\eta)\ d\xi d\eta \tag{5.38}$$

having $det\mathbf{J}$ defined as the relation between the area in the physical element and the master element, as both spaces are analysed counterclockwise, if the determinant of the Jacobian is positive, the transformation is correct. The computation of the element boundary integrals, relate to the numerical flux, is given by

$$\int_{\Gamma_{ei}} \mathbf{H}_{ei}\phi d\Gamma = \int_{-1}^{1} \mathbf{H}_{ei}\phi\left(\xi(\theta),\eta(\theta)\right) det\mathbf{J}_{ei} d\theta \tag{5.39}$$

where

$$d\Gamma = det\mathbf{J}_{ei}\, d\theta = \sqrt{\left(\frac{\partial x}{\partial \theta}\right)^2 + \left(\frac{\partial y}{\partial \theta}\right)^2}\, d\theta, \tag{5.40}$$

and the partial derivation is determined by

$$\frac{\partial x}{\partial \theta} = \frac{\partial x}{\partial \xi}\frac{\partial \xi}{\partial \theta} + \frac{\partial x}{\partial \eta}\frac{\partial \eta}{\partial \theta} \qquad \frac{\partial y}{\partial \theta} = \frac{\partial y}{\partial \xi}\frac{\partial \xi}{\partial \theta} + \frac{\partial y}{\partial \eta}\frac{\partial \eta}{\partial \theta} \tag{5.41}$$

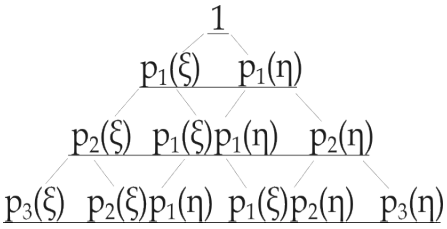

Figure 5.3: Pascal triangle of the basis functions

θ represents a parameterization of the triangular element's edges, where it assumes values between -1 and 1, as shown in equations 5.42[1]:

$$e^0_{ei}\begin{cases}\xi^0 = -\theta\\ \eta^0 = \theta\end{cases} \qquad e^1_{ei}\begin{cases}\xi^1 = -1\\ \eta^1 = -\theta\end{cases} \qquad e^2_{ei}\begin{cases}\xi^2 = \theta\\ \eta^2 = -1\end{cases} \tag{5.42}$$

As shown in figure 5.2, the parameter is applied in the master space, and it does not impact the physical space.

The outward normals $\mathbf{n}^p_{ei} = (n^p_x, n^p_y)$[1] on the edges of each triangle are determined in the Ω_e space, as shown in equation 5.43

$$n^p_x = \frac{1}{det\mathbf{J}_{ei}(\xi(\theta),\eta(\theta))}\frac{\partial x}{\partial \theta} \qquad n^p_y = -\frac{1}{det\mathbf{J}_{ei}(\xi(\theta),\eta(\theta))}\frac{\partial y}{\partial \theta} \tag{5.43}$$

Considering only the case of a triangle with straight edges the Jacobian is a constant along the edge however, it depends on the number of the edge.

5.4 Legendre polynomials and system of equation

Following the Legendre polynomials presented in chapter 4.4 for one-dimension, the two-dimension Legendre polynomial can be defined as a set of two-dimensional basis functions, defined in the interval [-1, 1]

$$\mathbf{q}(\xi,\eta,t) = \sum_{m=0}^{d+1}\phi_m(\xi,\eta)\,\mathbf{q}_m(t) \tag{5.44}$$

where $\mathbf{q}_m$ is the conservative vector, represented by

$$\mathbf{q}_m = (h_m \quad (hu)_m \quad (hv)_m) \tag{5.45}$$

and $(d+1)$ is the number of the basis functions based on the order k of the polynomial, it is given by

$$d+1 = \frac{1}{2}(k+1)(k+2) \tag{5.46}$$

this equation follows Pascal's triangle, shown in figure 5.3.

Since the set of basis functions is the product of the Legendre polynomial in ξ and η directions, the polynomial

[1] In the notation ξ^p of the equation 5.42 p exemplifies the edge number, which coincides with the opposite node, this indexing is used for the normal vectors as well

functions have to be orthonormal in the master element. Therefore, the norm and the inner product are respectively given by

$$||f(\xi,\eta)|| = \sqrt{\langle f(\xi,\eta), f(\xi,\eta)\rangle} \tag{5.47}$$

and

$$\langle f(\xi,\eta)\, g(\xi,\eta)\rangle = \int_{-1}^{1}\int_{-1}^{-\xi} f(x,y)\, g(x,y) det\mathbf{J} d\xi d\eta \tag{5.48}$$

Since the triangles are linear, the Jacobian is constant and the integral can be simplified as

$$\langle f(\xi,\eta)\, g(\xi,\eta)\rangle = \int_{-1}^{1}\int_{-1}^{-\xi} f(x,y)\, g(x,y) d\xi d\eta \tag{5.49}$$

where $f(\xi,\eta)$ and $g(\xi,\eta)$ are arbitrary functions in the domain X. In this case, the orthonormality is independent of the geometry of the element in the physical space. The modified Gram-Schmidt algorithm is presented by the following equations:

$$\phi_0 = \frac{\hat{\phi}_0}{||\hat{\phi}_0||}, \tag{5.50}$$

$$q_n = \sum_{i=0}^{n-1} \langle \tilde{\phi}_n, \phi_i\rangle\, \phi_i \tag{5.51}$$

and

$$\phi_n = \frac{\tilde{\phi}_n - q_n}{||\tilde{\phi}_n - q_n||} \tag{5.52}$$

where $n = 1, ..., d$, so every interaction m increases. Applying orthonormal vector ϕ_n to the equation 5.49 is obtained

$$\int_\Omega \phi_m \phi_n d\Omega = \int_{-1}^{1}\int_{-1}^{-\xi} \phi_m(\xi,\eta)\, \phi_n(\xi,\eta) d\eta d\xi = \delta_{mn} \tag{5.53}$$

Considering the Gram-Schmidt method in the set of basis functions of the master element, the first-order set of orthonormal Legendre functions is

$$\boldsymbol{\phi}_{1^{st}} = \begin{pmatrix} \frac{\sqrt{2}}{2} \\ \frac{3}{2}\xi + \frac{1}{2} \\ \frac{\sqrt{3}}{2}(2\eta + \xi + 1 \end{pmatrix}. \tag{5.54}$$

Bringing equations 5.40 and 5.53 as a smooth test functions into 5.7 gives

$$\begin{aligned} \frac{\partial \mathbf{q}_n}{\partial t} - \int_{\hat{\Omega}} \mathbf{F}(\mathbf{q})\cdot\nabla\phi_n d\xi d\eta + \sum_{\Gamma_e^{int}} \theta \int_{-1}^{1} \mathbf{H}(\mathbf{q}_{ei};\mathbf{q}_{ie};\mathbf{n}_{ei})\phi_n d\theta + \\ + \sum_{\Gamma_e^{bc}} \theta \int_{-1}^{1} \mathbf{H}(\mathbf{q}_{eb};\mathbf{q}_b^{bc};\mathbf{n}_{eb})\phi_n d\theta = \int_{\hat{\Omega}} \mathbf{s}\,\phi_n d\xi d\eta \end{aligned} \tag{5.55}$$

with $n = 0, ..., d$, it is important to notice that the Jacobians are constant since the triangle elements have straight edges, therefore they can be moved outside the integrals, $\theta = (det\mathbf{J})^{-1} det\mathbf{J}_{ei}$. [39]

The system can be written as

$$\frac{\partial \mathbf{q}_n}{\partial t} = \hat{\mathbf{F}}_n - \hat{\mathbf{H}}_n^{int} - \hat{\mathbf{H}}_n^{bc} + \hat{\mathbf{S}}_n = \boldsymbol{\mathcal{R}}_n(q) \tag{5.56}$$

where $\boldsymbol{\mathcal{R}}_n$ is defined as the residual, and it will be used in the chapter 5.6, and the other vectors are described by

$$\hat{\mathbf{F}}_n = \int_{-1}^{1} \int_{-1}^{-\xi} \mathbf{F}(\mathbf{q}) \cdot \nabla \phi_n d\xi d\eta \tag{5.57}$$

$$\hat{\mathbf{H}}_n^{int} = \sum_{\Gamma_e^{int}} \theta \int_{-1}^{1} \mathbf{H}(\mathbf{q}_{ei}; \mathbf{q}_{ie}; \mathbf{n}_{ei}) \phi_n d\theta \tag{5.58}$$

$$\hat{\mathbf{H}}_n^{bc} = \sum_{\Gamma_e^{bc}} \theta \int_{-1}^{1} \mathbf{H}(\mathbf{q}_{eb}; \mathbf{q}_b^{bc}; \mathbf{n}_{eb}) \phi_n d\theta \tag{5.59}$$

$$\hat{\mathbf{S}}_n = \int_{-1}^{1} \int_{-1}^{-\xi} \mathbf{s}\, \phi_n d\xi d\eta \tag{5.60}$$

5.5 Integrals discretization

The integration is computed on the master element by a two-dimensional Gaussian quadrature rule with g points (ξ, η) and weights w, the method applied in the flux gives

$$\hat{\mathbf{F}}_n = \sum_{b=1}^{g} w_b \left(\mathbf{F}_x(q(\xi_b, \eta_b)) \frac{\partial \phi_n(\xi_b, \eta_b)}{\partial x} + \mathbf{F}_y(q(\xi_b, \eta_b) \frac{\partial \phi_n(\xi_b, \eta_b)}{\partial y} \right) \tag{5.61}$$

where the partial derivation of ϕ_n is computed with the chain rule, as equation 5.30. The same procedure is practised on the source term,

$$\hat{s}_n = \sum_{b=1}^{g} w_b s(\xi_b, \eta_b) \phi_n(\xi_b, \eta_b) \tag{5.62}$$

The numerical flux regards only the edge, a one-dimensional element, therefore it is used the one-dimensional Gaussian quadrature rule with f points. In addition, θ-parametrisation is necessary to integrate along the edges. Applying the system in 5.42 onto the equations 5.58 and 5.59,

$$\hat{\mathbf{H}}_n^{int} = \sum_{\Gamma_e^{int}} \sum_{b=1}^{f} \theta w_b \mathbf{H}(\mathbf{q}_{ei}(\theta_b); \mathbf{q}_{ie}(-\theta_b); \mathbf{n}_{ei}) \phi_n(\theta_b) \tag{5.63}$$

$$\hat{\mathbf{H}}_n^{bc} = \sum_{\Gamma_e^{bc}} \sum_{b=1}^{f} \theta w_b \mathbf{H}(\mathbf{q}_{eb}(\theta_b); \mathbf{q}_b^{bc}(-\theta_b); \mathbf{n}_{eb}) \phi_n(\theta_b) \tag{5.64}$$

As q_{ei} and q_{ie} are related to the same edge, but considered in the two opposite directions, likewise $\pm\theta$ in q_{ei} have the opposite direction $\mp\theta$ in q_{ie}. [39]

5.6 Time integration

$\boldsymbol{\mathcal{R}}_n(q)$ is necessary for the discretization in time of the system of equations 5.56, an explicit third-order total variation diminishing (TVD) Runge-Kutta method is has been used as follows:

$$\begin{aligned} q_n^{(1)} &= q_n^{(0)} + \Delta t \boldsymbol{\mathcal{R}}_n(q^{(0)}) \\ q_n^{(2)} &= \frac{3}{4} q_n^{(0)} + \frac{1}{4} q_n^{(1)} + \frac{1}{4} \Delta t \boldsymbol{\mathcal{R}}_n(q^{(1)}) \\ q_n^{(3)} &= \frac{1}{3} q_n^{(0)} + \frac{2}{3} q_n^{(2)} + \frac{2}{3} \Delta t \boldsymbol{\mathcal{R}}_n(q^{(2)}) \end{aligned} \tag{5.65}$$

where superscript numbers are the progression in time and zero refers to the initial condition imposed. Stable conditions are verified by

$$\Delta t \leq \frac{\sqrt{(A_{\Omega_e})_{min}}\, f_1}{\lambda_{max}} CFL \tag{5.66}$$

with $(A_{\Omega_e})_{min}$ is the element Ω_e with the smallest area in the physical space, CFL is Courant-Friedrichs-Lewy number which is defined between 0 and 1, and λ_{max} and f_1 are given by

$$\lambda_{max} = ||\mathbf{v} \cdot \mathbf{v}|| + c \tag{5.67}$$

$$f_1 = (2k+1)^{-1} \tag{5.68}$$

The solution reaches a convergence when the residual tends to zero.[39]

5.7 Boundary conditions

In this case, there are 3 boundary conditions to consider: the side walls, the inlet flow and the outlet depth.
The boundary condition of the slide wall between the elements Ω_e and the limit of the space analysed represented by Ω_b^{bc}, which is a ghost cell, is determined as $u = 0$ on the edge between the two elements. This condition is specified by the calculation of the flow rate normal to the boundary

$$q_{eb}^n = (q_{eb} \cdot \hat{n}_{eb}) \hat{n}_{eb} \tag{5.69}$$

and reflecting the state of the ghost cell as

$$q_{be}^{bc,wl} = (h_{eb} \quad -q_{eb}^n) \tag{5.70}$$

It is significant to underline that these data come from the inner space, so $h_{eb} = h_{be}$. The numerical flux is defined by

$$H_{eb} = H(q_{eb}, q_{be}^{bc,wl}, \hat{n}_{eb}). \tag{5.71}$$

The inlet boundary related to the flow rate at the interface between Ω_e and Ω_b^{bc} takes into consideration only the

normal component of the inlet flow rate to the boundary element,

$$q_{in}^{n} \;=\; (q_{in} \cdot \hat{n}_{be})\hat{n}_{be} \tag{5.72}$$

thus shown on the ghost cell as

$$q_{be}^{bc,in} \;=\; (h_{eb} \quad q_{in}^{n}) \tag{5.73}$$

As in the previous condition, the depth is defined for the ghost cell by the inner element. The numerical flux boundary is given by

$$H_{eb} \;=\; H(q_{eb}, q_{be}^{bc,in}, \hat{n}_{eb}). \tag{5.74}$$

The outlet boundary related to the water depth at the interface between Ω_e and Ω_b^{bc} is established by the ghost cell state

$$q_{be}^{bc,ou} \;=\; (h_{be} \quad q_{ou}) \tag{5.75}$$

Similarly to the inlet and the wall boundaries, the flow rate is defined by the inner element, therefore $q_{ou} = q_{eb} = q_{be}$. The numerical flux boundary is given by

$$H_{eb} \;=\; H(q_{eb}, q_{be}^{bc,ou}, \hat{n}_{eb}). \tag{5.76}$$

In all the three cases, q_{eb}, q_{in}, q_{ou} are define by the two components of the velocity

$$q \;=\; h\mathbf{v} \;=\; \begin{pmatrix} hu \\ hv \end{pmatrix} \tag{5.77}$$

5.8 Computational implementation

In the 2D case, two sets of functions take place to determine the solution: the geometrical transformation (eq. 5.26) and the polynomial approximation of the solution (eq. 5.44), and generally, they have the same degree of approximation, even though it is not mandatory.

5.8.1 Element integration

The conservative set of variables of equation 5.44 for each element can be expressed in a matrix form

$$\mathbf{q}(\xi, \eta, t) \;=\; \sum_{m=0}^{d+1} \sum_{l=1}^{g} \phi_m(\xi_b, \eta_b)\, \mathbf{q}_m(t) \;=\; (\mathbf{\Phi}(\xi, \eta))^T\, \hat{q}(t) \tag{5.78}$$

with $0 < m < d$ and $1 < b < g$, which determined the matrix $\mathbf{\Phi}(\xi, \eta)$ and $\hat{q}(t)$

$$\mathbf{\Phi}(\xi,\eta) = \begin{pmatrix} \phi_0(\xi_1,\eta_1) & \phi_0(\xi_2,\eta_2) & ... & \phi_0(\xi_g,\eta_g) \\ \phi_1(\xi_1,\eta_1) & \phi_1(\xi_2,\eta_2) & ... & \phi_1(\xi_g,\eta_g) \\ ... & ... & ... & ... \\ \phi_d(\xi_1,\eta_1) & \phi_d(\xi_2,\eta_2) & ... & \phi_d(\xi_g,\eta_g) \end{pmatrix} \tag{5.79}$$

$$\hat{q}(t) = \begin{pmatrix} h_0 & (hu)_0 & (hv)_0 \\ h_1 & (hu)_1 & (hv)_1 \\ ... & ... & ... \\ h_d & (hu)_d & (hv)_d \end{pmatrix} = \begin{pmatrix} q_0^T \\ q_1^T \\ ... \\ q_d^T \end{pmatrix} \tag{5.80}$$

The flux equation 5.61 in a matrix form is given by

$$\hat{F} = \frac{1}{J}\left(\frac{d\Phi}{dx}\,(W \odot F_x) + \frac{d\Phi}{dy}\,(W \odot F_y)\right) \tag{5.81}$$

where

$$\frac{\mathbf{\Phi}}{dx} = \begin{pmatrix} \frac{\partial \phi_0^e}{\partial x}(\xi_1,\eta_1) & \frac{\partial \phi_0^e}{\partial x}(\xi_2,\eta_2) & ... & \frac{\partial \phi_0^e}{\partial x}(\xi_g,\eta_g) \\ \frac{\partial \phi_1^e}{\partial x}(\xi_1,\eta_1) & \frac{\partial \phi_1^e}{\partial x}(\xi_2,\eta_2) & ... & \frac{\partial \phi_1^e}{\partial x}(\xi_g,\eta_g) \\ ... & ... & ... & ... \\ \frac{\partial \phi_d^e}{\partial x}(\xi_1,\eta_1) & \frac{\partial \phi_d^e}{\partial x}(\xi_2,\eta_2) & ... & \frac{\partial \phi_d^e}{\partial x}(\xi_g,\eta_g) \end{pmatrix}, \tag{5.82}$$

$$W = \begin{pmatrix} w_1 \\ w_2 \\ ... \\ w_g \end{pmatrix}, \tag{5.83}$$

$$F_x = \begin{pmatrix} F_x^T(\mathbf{q}_1) \\ F_x^T(\mathbf{q}_2) \\ ... \\ F_x^T(\mathbf{q}_g) \end{pmatrix} \tag{5.84}$$

and $\frac{d\Phi}{dy}$ e F_y have the same form of $\frac{d\Phi}{dx}$ e F_x. It is important to notice that $\odot$ is a symmetric product, so it is a linear product between the elements of the vector and the matrix. The derivatives of the basis functions are given by

$$\frac{\partial \phi_m^e}{\partial x} = \frac{\partial \phi_m}{\partial \xi}\frac{\partial \xi}{\partial x} + \frac{\partial \phi_m}{\partial \eta}\frac{\partial \eta}{\partial x} \qquad \frac{\partial \phi_m^e}{\partial y} = \frac{\partial \phi_m}{\partial \xi}\frac{\partial \xi}{\partial y} + \frac{\partial \phi_m}{\partial \eta}\frac{\partial \eta}{\partial y} \tag{5.85}$$

Following the same procedure, the source terms are defined as

$$\hat{s} = \Phi\,(W \odot S) \tag{5.86}$$

with

$$S = \begin{pmatrix} s^T(\mathbf{q}_1) \\ s^T(\mathbf{q}_2) \\ \dots \\ s^T(\mathbf{q}_g) \end{pmatrix} \tag{5.87}$$

5.8.2 Edge integration

The edge integrals have a separate analysis from the inner part of the element. As they have a parameterization and are one dimensional, the conservative variables $\mathbf{q}$ need to be computed for p points, as follows

$$\mathbf{q}^{ed}(\xi, \eta, t) = (\mathbf{\Phi}_{ei}^{p^{ed}}(\xi, \eta))^T \hat{q}(t) \tag{5.88}$$

where Φ follows the indexing system presented in the parameterization, equation 5.42, and figure 5.1, further the superscript ed indicates that the calculations are related to the edges of the master element.

$$\mathbf{\Phi}_{ei}^{p^{ed}} = \begin{pmatrix} \phi_0(\xi_{\theta_1}^p, \eta_{\theta_1}^p) & \phi_0(\xi_{\theta_2}^p, \eta_{\theta_2}^p) & \dots & \phi_0(\xi_{\theta_f}^p, \eta_{\theta_f}^p) \\ \phi_1(\xi_{\theta_1}^p, \eta_{\theta_1}^p) & \phi_1(\xi_{\theta_2}^p, \eta_{\theta_2}^p) & \dots & \phi_1(\xi_{\theta_f}^p, \eta_{\theta_f}^p) \\ \dots & \dots & \dots & \dots \\ \phi_d(\xi_{\theta_1}^p, \eta_{\theta_1}^p) & \phi_d(\xi_{\theta_2}^p, \eta_{\theta_2}^p) & \dots & \phi_d(\xi_{\theta_f}^p, \eta_{\theta_f}^p) \end{pmatrix} \tag{5.89}$$

Therefore the numerical fluxes are represented by

$$\hat{H}_{ei} = \hat{H}_{ei}^p = \frac{1}{J} \Phi_{ei}^p \left(W^{ed} \odot H_{ei}^p \right) \tag{5.90}$$

where

$$W^{ed} = \begin{pmatrix} w_1 \\ w_2 \\ \dots \\ w_f \end{pmatrix} \tag{5.91}$$

and

$$H_{ei}^{p^{ed}} = \begin{pmatrix} H_{ei}^T(\mathbf{q}_1^{ed}) \\ H_{ei}^T(\mathbf{q}_2^{ed}) \\ \dots \\ H_{ei}^T(\mathbf{q}_f^{ed}) \end{pmatrix} \tag{5.92}$$

The only matrix equal all along the computation is $\hat{q}(t)$ because it depends only on time.

5.8.3 Time integration

The Runge-Kutta method for the time discretization presented in the set of equations 5.65 is determined by

$$\begin{aligned}
\hat{q}^{(1)} &= \hat{q}^{(0)} + \Delta t\, \boldsymbol{\mathcal{R}}(\hat{q}^{(0)}) \\
\hat{q}^{(2)} &= \frac{3}{4}\hat{q}^{(0)} + \frac{1}{4}\hat{q}^{(1)} + \frac{1}{4}\Delta t\, \boldsymbol{\mathcal{R}}(\hat{q}^{(1)}) \\
\hat{q}^{(3)} &= \frac{1}{3}\hat{q}^{(0)} + \frac{2}{3}\hat{q}^{(2)} + \frac{2}{3}\Delta t\, \boldsymbol{\mathcal{R}}(\hat{q}^{(2)})
\end{aligned} \tag{5.93}$$

with

$$\boldsymbol{\mathcal{R}} = \hat{F} - \hat{H} + \hat{s} \tag{5.94}$$

Chapter 6

Numerical results

6.1 One-dimensional cases

The one-dimensional code has three main variables to verify the accuracy of the solution: the degree of the polynomial, the number of Gauss points and the number of elements present in the mesh.

It has been considered the channel length of 20'000 metres and the seabed without friction. The initial conditions

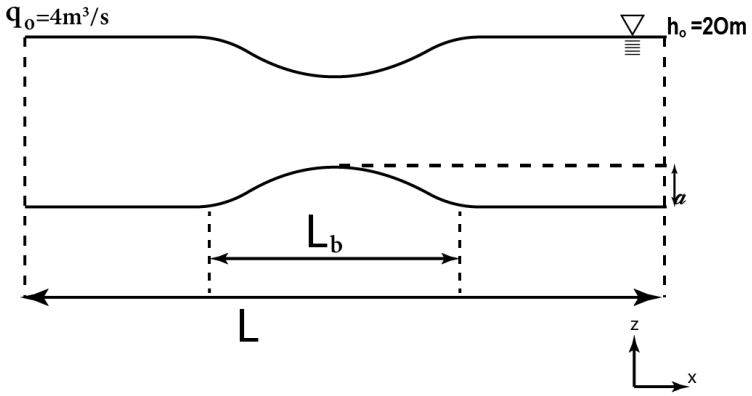

Figure 6.1: Channel with a bump and the final resolution expected.

are a water depth of 20 m downstream and a flow rate of 4 m^3/s upstream. This case has been studied with a bump in the bathymetry. The bump was obtained through two different equations: a parabola and a sinusoidal equation

$$f(x) = \frac{a}{2}\left(cos\left(\frac{2\pi(x-x_0)}{L_b}\right)+1\right) \tag{6.1}$$

$$f(x) = a\left(1-\frac{4(x-x_0)^2}{L_b^2}\right) \tag{6.2}$$

where a is the amplitude or the height of the bump of 2 m, L_b is the length of the bump of 10'000 m and x_0 is the centre of the bump in the centre of the channel.

The two equations represent the same bump, but the difference is in conjunction with the flat seabed. The parabola has a sharp angle while the sinusoidal function has a more regular joining.

The results from the simulation with the parabola equation, for different even numbers of elements and Gauss-Legendre points, are shown in figures 6.2 to 6.5. The water surface results are accurately predicted even with a few elements and Gauss-Legendre points. While, the flow rate shows an oscillation, which reduces its intensity with the increase in the number of elements and Gauss-Legendre points. The last result, figure 6.5, is the best solution achieved during the analysis, in terms of local error.

Other solutions with the sinusoidal bump and the parabola bump are shown in Appendix B.

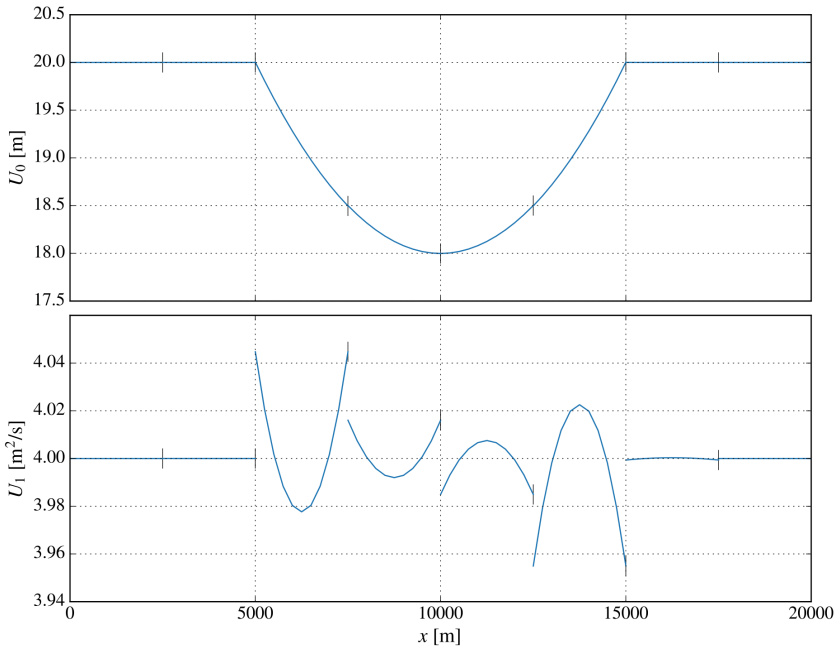

Figure 6.2: Solution with 8 elements, the second order of polynomial and 2 Gauss-Legendre points, with parabola bump function.

6.1.1 Error evaluation

Figures from 6.6a to 6.6c show the discretization error as a function of the mesh size, with different numbers of Gauss-Legendre points.

U_0, which represents the water depth, achieves a high level of accuracy in all cases. When U_1, which is the flow rate, a higher number of Gauss-Legendre points is needed to obtain the expected error decadence. These behaviours are shown in the higher polynomial orders in Appendix C.

Considering the better results are errors for U_0. Therefore, the different numbers of Gauss-Legendre points were compared, and the best trend line is shown. It is important to point out that the minimum number of Gauss-Legendre points that can be exploited is equal to the degree of the polynomial g. Otherwise there are not enough points to solve the polynomial.

The lowest error related to the number of elements is achieved with the number of points equal to $g+1$, however, this case never represents the finest error decay. The increase in the number of Gauss-Legendre points does not generate a consistent variation in the error after the $g+3$, as shown in figure 6.8. There is only a consistent improvement in the error associated with the increase in Gauss-Legendre points, from two to three or four points, which becomes negligible with the fourth degree of the polynomial, as shown in figure 6.9.

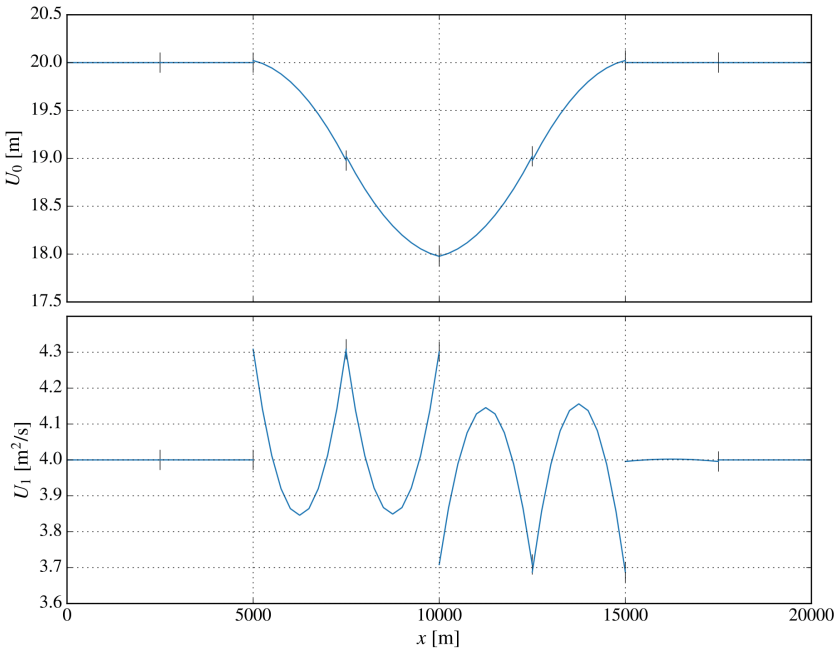

Figure 6.3: Solution with 8 elements, the second order of polynomial and 4 Gauss-Legendre points, with sinusoidal bump function.

Comparing the three graphs 6.7, 6.8 and 6.9, the increase of the polynomial degree minimises the error and the model requires a lower number of elements.

The fifth order of the polynomial has been studied, but it does not present good results due to the round-off errors, the results are shown in appendix C.

The solution has been studied with odd numbers of elements as well. Understanding of the effects of bathymetry when the variation from the flat seabed to the bump is within an element. The results show that the sinusoidal function gives a better degree of accuracy. As the function creates a more regular transition from the flat seabed to the bump, as it is possible to see in figure 6.3. Instead, the parabola function creates a sharp corner inside the element. All the previous considerations are valid for the error of the odd numbers of elements, even if the error trends do not show the decadence expected.

6.2 Two-dimensional cases

In the two-dimensional code has been considered the channel length of 20'000 m, the width of 4'000 m and the seabed is without friction. The mesh has a refinement of 250 m. It is shown in figure 6.11 with the boundary conditions.

The initial conditions are a water depth of 20 m downstream, named in figure 6.11 a BC100, a flow rate of 4 m^3/s upstream, called BC101 and a boundary condition at the wall of zero velocity, named BC102. These conditions describe a sub-critical flow.

It is important to notice that the Gauss-Legendre points are divided in internal and on the edges. The minimum number of Gauss-Legendre points inside the element in this case is 3, due to the second dimension. Moreover, there is a different correlation from the 1D model between the degree of the polynomial and the internal Gauss-Legendre

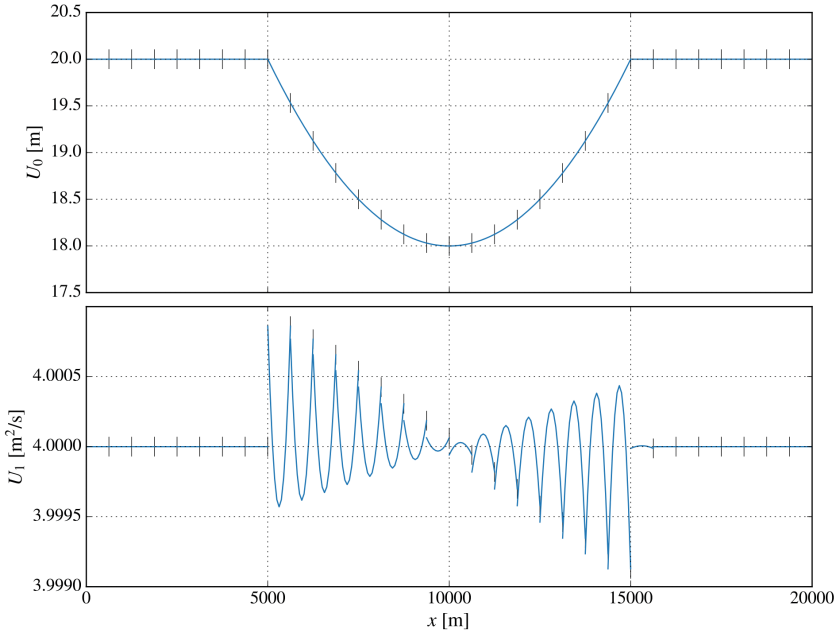

Figure 6.4: Solution with 32 elements, the second order of polynomial and 2 Gauss-Legendre points, with parabola bump function.

points given by the quadrature rule.

The water surface results are accurately predicted in all cases run with different Gauss-Legendre points and degrees of polynomial. While the flow rate shows a decrease in accuracy with the increase of the polynomial, this unexpected result may be related to an error in the code. However, it was not found it.

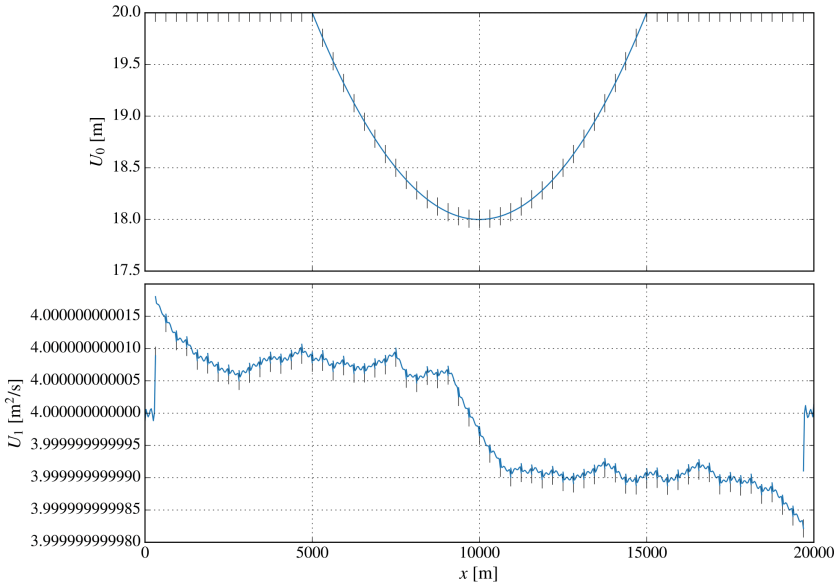

Figure 6.5: Solution with 128 elements, second order of polynomial and 4 Gauss-Legendre points, with a sinusoidal function for the bump.

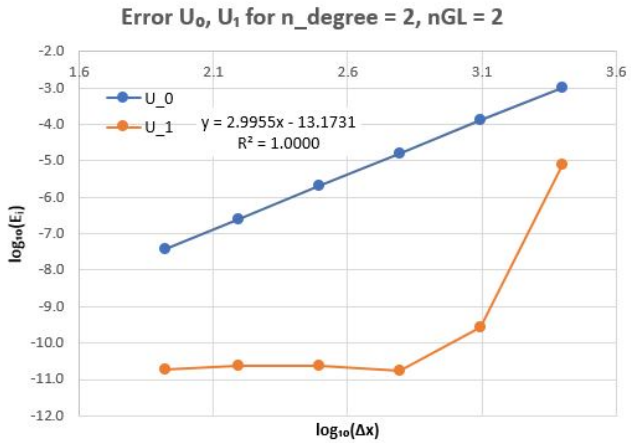

(a)

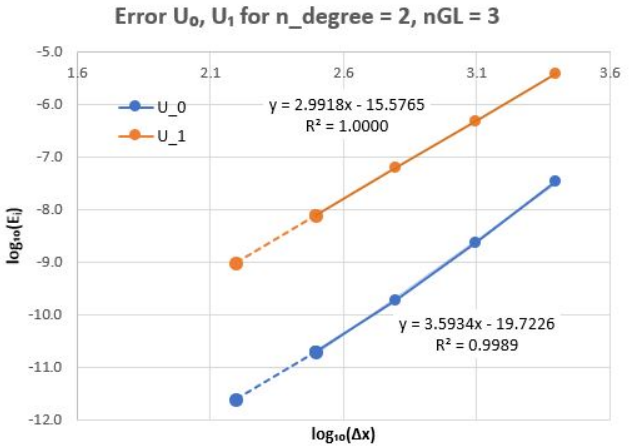

(b)

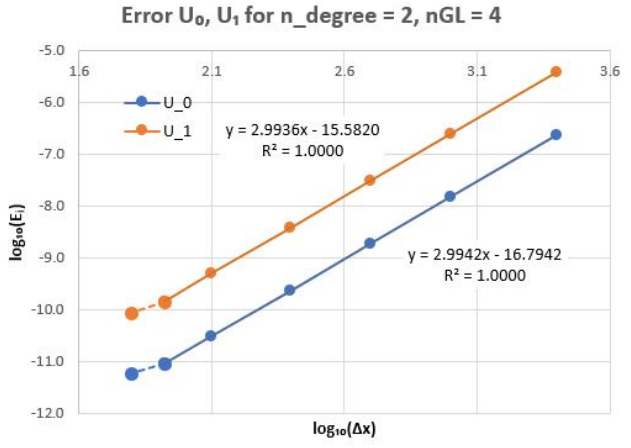

(c)

Figure 6.6: Error of U_0 and U_1 with even numbers of elements, the second order of polynomial: (a) 2 Gauss-Legendre points, (b) 3 Gauss-Legendre points and (c) 4 Gauss-Legendre points.

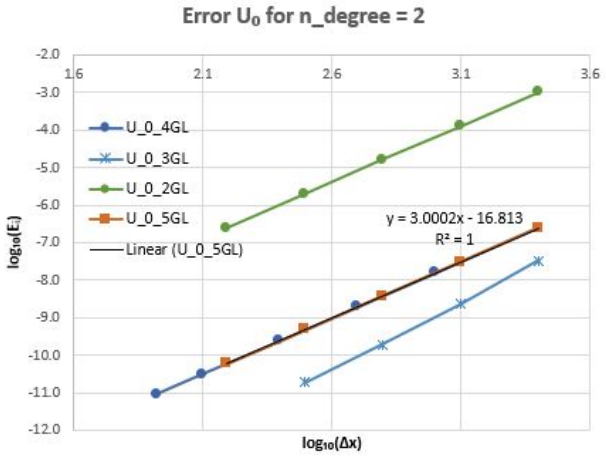

Figure 6.7: Comparison of the errors of U_0 of the second-order polynomial with different Gauss-Legendre points even number of elements and a parabola as bump function.

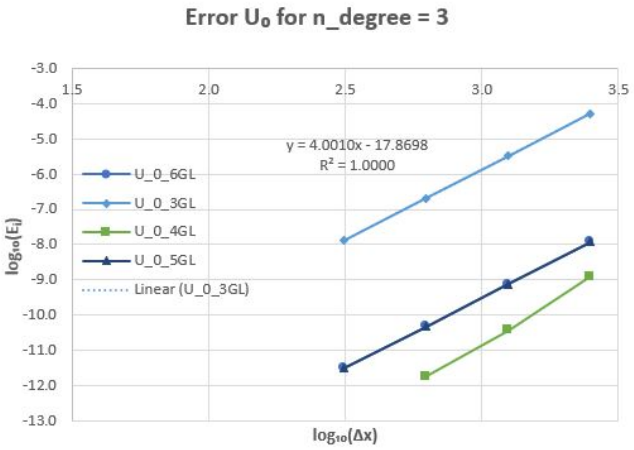

Figure 6.8: Comparison of the errors of U_0 of the third-order polynomial with different Gauss-Legendre points even number of elements and a parabola as bump function.

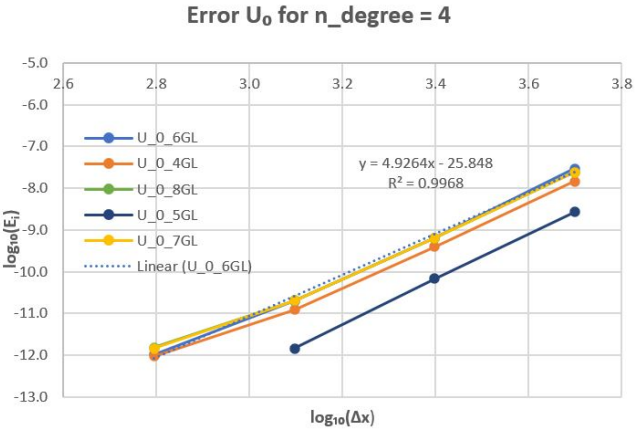

Figure 6.9: Comparison of the errors of U_0 of the fourth-order polynomial with different Gauss-Legendre points even number of elements and a parabola as bump function.

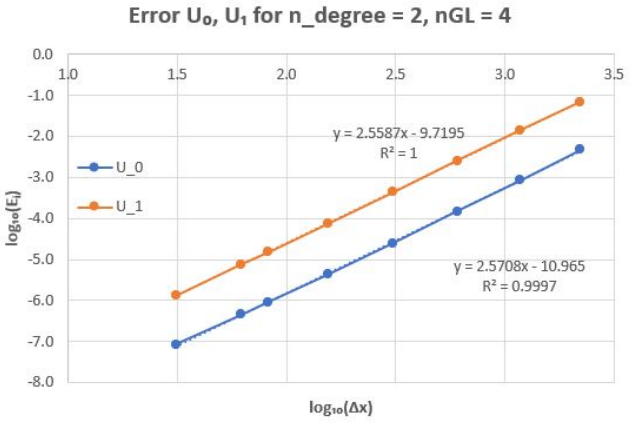

(a)

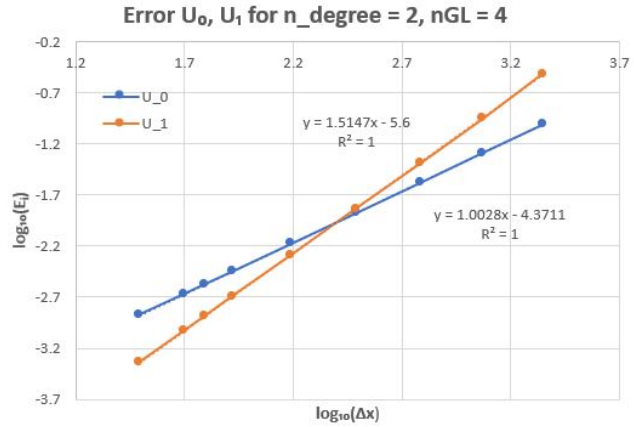

(b)

Figure 6.10: Error of U_0 and U_1 with odd numbers of elements: (a) the sinusoidal function for the bump and (b) the parabola function for the bump

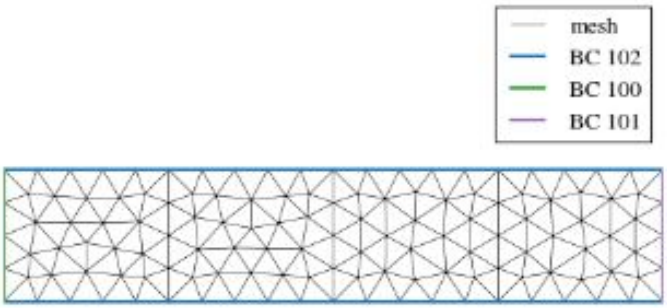

Figure 6.11: Mesh applied in the 2D code.

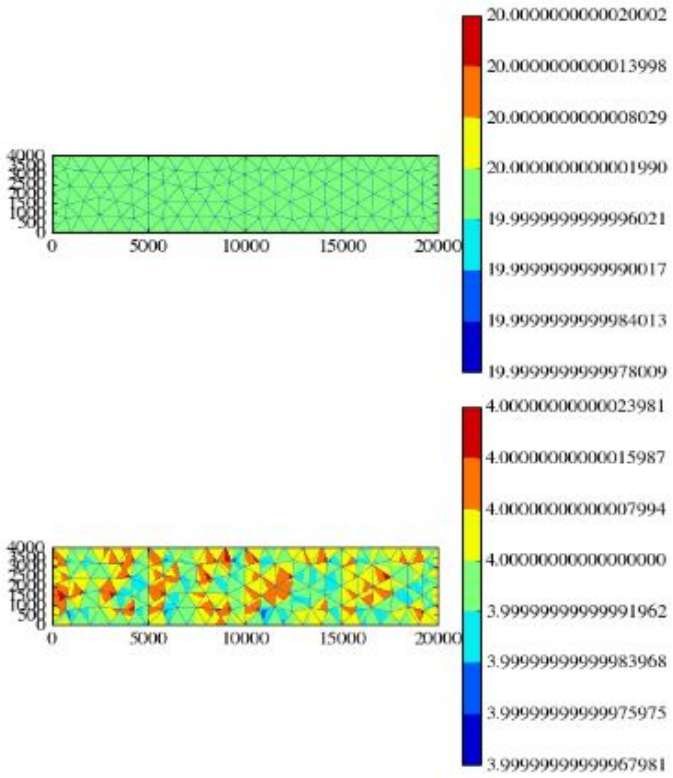

Figure 6.12: Solution with second order of polynomial and 4 Gauss-Legendre points internal and on the edges.

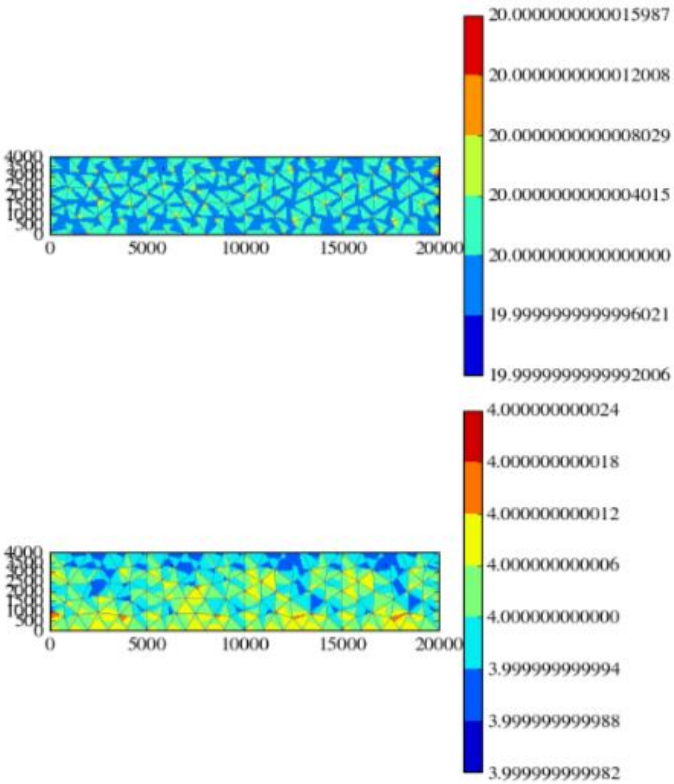

Figure 6.13: Solution with the fourth order of polynomial and 4 Gauss-Legendre points internal and on the edges.

Chapter 7

Conclusions

The recent development of new turbine technologies opens new possibilities for the extraction of energy from tidal flow. Compared to other renewable energies, tidal power has considerable advantages. Its predictability enables the resource to be accurately quantified, unlike stochastic energy sources. It has a low environmental impact and no occupation of land.

This thesis studied the tidal resource assessment procedure for the situation of the current projects and developed a numerical method to analyse tidal hydrodynamics. The numerical method selected was the Discontinuous Galerkin method. Since it has the ability to use unstructured meshes and to model flows with significant horizontal velocities. In addition to the boundary condition directly implemented numerical flux, and provides higher accuracy within the flow field. This tool has a one-dimensional and two-dimensional versions.

The one-dimensional model developed presents the correct computation of the flow rate, the momentum flux in the local field and the water depth in all cases studied and presented. The precision of the model is confirmed by the error analysis, which is minimised by the refinement of the mesh and the increase of the polynomial order. This follows the theory, until the fifth order of the polynomial, where the round-off error starts to overcome the discretization error.

The two-dimensional model presents the correct computation of the flow rate, the momentum flux in the local field and the water depth in the case studied. However, the accuracy decrease and the residual increase with the increase in the polynomial degree, which suggests a problem in the code.

In summary, the numerical model has been proved useful for estimating the tidal stream's local velocities and water depth, in one-dimensional and two-dimensional. It can potentially be applied for tidal resource assessment and energy extraction analysis.

7.1 Future research

This work can be further develop in the two-dimensional code with the more theoretical study. It is possible the application to a real case scenario with the bathymetry, for example the Bristol Channel, to present a tidal energy resource assessment. The model could include a turbine or an array, in order to study the energy extraction of a real

case scenario. The model can be enriched and become more realistic with the introduction of the bottom friction in the source terms.

Bibliography

[1] Sadeq Alfakih et al. “Simulation model of single structured tower hybrid wind and tidal energy cultivation based on Yemen’s south west coast”. In: vol. 107. June 2019. DOI: 10.1051/e3sconf/201910701007.

[2] S.C. Bhatia. “13 - Tide, wave and ocean energy”. In: *Advanced Renewable Energy Systems*. Ed. by S.C. Bhatia. Woodhead Publishing India, 2014, pp. 307–333. ISBN: 978-1-78242-269-3. DOI: https://doi.org/10.1016/B978-1-78242-269-3.50013-9. URL: https://www.sciencedirect.com/science/article/pii/B9781782422693500139.

[3] Alexander Claude Brown and Anton McLachlan. *The ecology of sandy shores*. Elsevier, 2010.

[4] R.H. Charlier and C.W. Finkl. *Ocean Energy: Tide and Tidal Power*. Earth and Environmental Science. Springer Berlin Heidelberg, 2009. ISBN: 9783540779322. URL: https://books.google.com.pe/books?id=RKbWnCckHcwC.

[5] R. H. Clark and Sarah-taissir Bencharif. “Tidal Energy”. In: (2015). URL: https://www.thecanadianencyclopedia.ca/en/article/tidal-energy.

[6] World Energy Council. *Survey of Energy Resources*. 2010.

[7] S. Draper. “Tidal stream energy extraction in coastal basins”. PhD thesis. Oxford University, UK, 2011.

[8] EMEC. *Tidal devices*. 2022. URL: https://www.emec.org.uk/marine-energy/tidal-devices/.

[9] Amir Garanovic - Offshore Energy. *MeyGen set for additional 28MW of tidal energy*. URL: https://www.offshore-energy.biz/meygen-set-for-additional-28mw-of-tidal-energy/.

[10] Amir Garanovic - Offshore Energy. *Verdant Power’s tidal turbine array exceeds expectations*. URL: https://www.offshore-energy.biz/verdant-powers-tidal-turbine-array-exceeds-expectations/.

[11] SIMEC Atlantis Energy. *MeyGen*. URL: https://simecatlantis.com/projects/meygen/.

[12] Edinburgh University - School of Engineering. *Tidal Energy Potential of Pentland Firth Revealed*. URL: https://www.eng.ed.ac.uk/about/news/20140128/tidal-energy-potential-pentland-firth-revealed.

[13] Ocean Energy Europe. *Sabella*. URL: https://www.oceanenergy-europe.eu/annual/sabella/.

[14] R. D. Ray G. D. Egbert. “Estimates of tidal energy dissipation from TOPEX/Poseidon altimeter data”. In: (2001).

[15] Chris Garrett and Patrick Cummins. “Generating Power from Tidal Currents”. In: *Journal of Waterway Port Coastal and Ocean Engineering-asce - J WATERW PORT COAST OC-ASCE* 130 (May 2004). DOI: 10.1061/(ASCE)0733-950X(2004)130:3(114).

[16] Chris Garrett and Patrick Cummins. “The power potential of tidal currents in channels”. In: *Proceedings of The Royal Society A: Mathematical, Physical and Engineering Sciences* 461 (Aug. 2005), pp. 2563–2572. DOI: 10.1098/rspa.2005.1494.

[17] Open Energy Information. *Nova M100*. URL: https://openei.org/wiki/PRIMRE/Databases/Projects_Database/Devices/Nova_M100.

[18] Nova Innovation. *Europe Case Study - Shetland Tidal Array*. URL: https://www.novainnovation.com/markets/scotland-shetland-tidal-array/.

[19] Gaia Innovations. *Flumill – harvesting tidal energy*. URL: https://www.gaiainnovations.org/innovation/flumill-harvesting-tidal-energy/.

[20] R. A. Plumb J. Marshall. *Atmosphere, Ocean and Climate Dynamics*. Academic Press, 2007.

[21] Woowon Jeong and Jaehoon Seong. “Comparison of effects on technical variances of computational fluid dynamics (CFD) software based on finite element and finite volume methods”. In: *International Journal of Mechanical Sciences* 78 (2014), pp. 19–26. ISSN: 0020-7403. DOI: https://doi.org/10.1016/j.ijmecsci.2013.10.017. URL: https://www.sciencedirect.com/science/article/pii/S002074031300297X.

[22] Abdul Khan and Wencong Lai. *Modeling Shallow Water Flows Using the Discontinuous Galerkin Method*. Mar. 2014. ISBN: 9780429157936. DOI: 10.1201/b16579.

[23] P.D. Komar. *Beach Processes and Sedimentation*. Prentice Hall, 1998.

[24] Minesto. *Minesto’s tidal power plant in grid-connected operation - commercial performance verified*. URL: https://minesto.com/news-media/minestos-tidal-power-plant-grid-connected-operation-commercial-performance-verified?utm_source=Tethys&utm_campaign=30ec6cb14c-Tethys+Engineering+Blast+15+July+2022&utm_medium=email&utm_term=0_2d9450ca22-30ec6cb14c-451629636.

[25] Minesto. *The future of renewable energy*. URL: https://minesto.com/our-technology.

[26] Minesto. *The future of renewable energy*. URL: https://minesto.com/our-technology.

[27] L. Myers et al. “Inter-device spacing issues within wave and tidal energy converter arrays”. In: (2010).

[28] P Novak et al. *Hydraulic Modelling - an Introduction*. Jan. 2010. ISBN: 0-419-25010-7 (hbk); 0-419-25020-4 (pbk); 0-203-86162-0 (ebk).

[29] OpenEI. *CoRMaT*. URL: https://openei.org/wiki/PRIMRE/Databases/Projects_Database/Devices/CoRMaT.

[30] OpenEI. *PLAT-I*. URL: https://openei.org/wiki/PRIMRE/Databases/Projects_Database/Devices/PLAT-I.

[31] Joaquim Peiro and Spencer Sherwin. "Finite difference, finite element, and finite volume method". In: *Handbook of Materials Modeling, Volume I, Methods and Models* (Jan. 2005), pp. 1–32.

[32] D.T. Pugh. *Tides, Surges and Mean Sea-Level*. John Wiley and Sons, 1987.

[33] Bastian E. Rapp. "Chapter 31 - Finite Volume Method". In: *Microfluidics: Modelling, Mechanics and Mathematics*. Ed. by Bastian E. Rapp. Micro and Nano Technologies. Oxford: Elsevier, 2017, pp. 633–654. ISBN: 978-1-4557-3141-1. DOI: https://doi.org/10.1016/B978-1-4557-3141-1.50031-9. URL: https://www.sciencedirect.com/science/article/pii/B9781455731411500319.

[34] P. J. Roache. *Fundamentals of verification and validation*. Hermosa Publishers, Mar. 2009.

[35] Morag Robertson et al. "OPTIMISATON AND ENHANCEMENT OF TIDAL ENERGY DEVICES". In: Nov. 2021.

[36] Sabella. *Sabella D10 - FRANCE*. URL: sabella.bzh/en/projects/d10.

[37] Abdusamad A. Salih. *Finite Element Method*.

[38] Seetao. *Zhejiang Zhoushan tidal energy power station successfully launched*. URL: https://www.seetao.com/details/141111.html (visited on 02/28/2022).

[39] Irving H. Shames. *Mechanics of Fluids*. McGraw-Hill, International Student Edition, 1982.

[40] G. I. Taylor. "Tidal Friction in the Irish Sea". In: *Journal of Geophysical Research* (1920).

[41] Power technology. *SeaGen Turbine, Northern Ireland, UK*. URL: https://www.power-technology.com/projects/strangford-lough/.

[42] Tethys. *Cobscook Bay Tidal Energy Project*. URL: https://tethys.pnnl.gov/project-sites/cobscook-bay-tidal-energy-project.

[43] Tethys. *Kvalsund Tidal Turbine Prototype*. URL: https://tethys.pnnl.gov/project-sites/kvalsund-tidal-turbine-prototype.

[44] Tethys. *MeyGen Tidal Energy Project - Phase I*. URL: https://tethys.pnnl.gov/project-sites/meygen-tidal-energy-project-phase-i.

[45] Tethys. *Nova Innovation - Shetland Tidal Array*. URL: https://tethys.pnnl.gov/project-sites/nova-innovation-shetland-tidal-array.

[46] Tethys. *Roosevelt Island Tidal Energy (RITE) Project Pilot*. URL: https://tethys.pnnl.gov/project-sites/roosevelt-island-tidal-energy-rite-project-pilot.

[47] Tethys. *Sabella D10 tidal turbine at Ushant Island*. URL: https://tethys.pnnl.gov/project-sites/sabella-d10-tidal-turbine-ushant-island.

[48] Tethys. *ScotRenewables SR2000 at EMEC*. URL: https://tethys.pnnl.gov/project-sites/scotrenewables-sr2000-emec.

[49] Tethys. *Strangford Lough - MCT (SeaGen)*. URL: https://tethys.pnnl.gov/project-sites/strangford-lough-mct-seagen.

[50] Tethys. *Tidal Current Energy Developments Highlights*. URL: https://tethys-engineering.pnnl.gov/sites/default/files/publications/Tidal-Current-Energy-Highlights.pdf.

[51] Tethys. *Western Passage Tidal Energy Project*. URL: https://tethys.pnnl.gov/project-sites/western-passage-tidal-energy-project.

[52] C Vogel. "Theoretical limits to tidal stream energy extraction". PhD thesis. Oxford University, UK, 2014.

[53] Roy A. Walters, Michael R. Tarbotton, and Clayton E. Hiles. "Estimation of tidal power potential". In: *Renewable Energy* 51 (2013), pp. 255–262. ISSN: 0960-1481. DOI: https://doi.org/10.1016/j.renene.2012.09.027. URL: https://www.sciencedirect.com/science/article/pii/S0960148112005988.

Appendix A

Study case: Channel over a bump

A case is considered a steady flow in a channel with constant width over a bump. The channel width is d, ζ is the free surface height, b is the channel bathymetry and the water depth is represented by $h = \zeta - b$.

This analysis has the purpose of understanding the steady flow behaviour. The area can be divided into two portions,

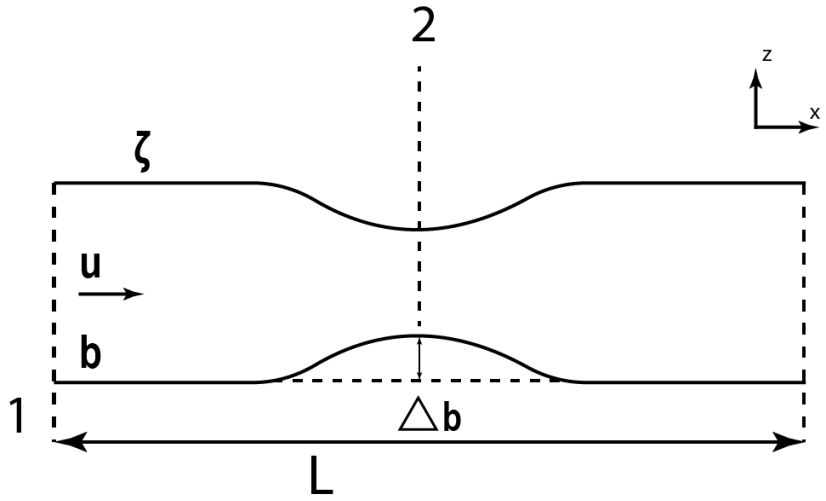

Figure A.1: Channel with a bump divided into two sections.

the first portion is upstream of the highest point of the bump and the second section is downstream of the highest point. Since the mass balance must be respected, the flow rate is constant. This implies a variation of the momentum between the two areas due to the bump. The free surface momentum between the two stages can be written as

$$h_1 + \frac{u_1^2}{2g} = \frac{u_2^2}{2g} + \Delta b \tag{A.1}$$

where Δb is the bump height and the specific energy is given by

$$E = h + \frac{u^2}{2g}. \tag{A.2}$$

If the equation is expressed as a function of the flow rate, it is obtained

$$q = h\sqrt{2g(E-h)} \tag{A.3}$$

This equation demonstrates that the water depth has an upper and lower limit, $0 < h < E$.

The flow rate must be constant along the channel because of the conservation of mass under steady-state conditions.

Reformulating the equation A.1 as

$$E_2 = E_1 - \Delta b \tag{A.4}$$

Therefore, it is possible to determine the exact water depth to compare the exact solution to the numerical method in the code developed.

Appendix B

Plots of the one-dimensional solutions

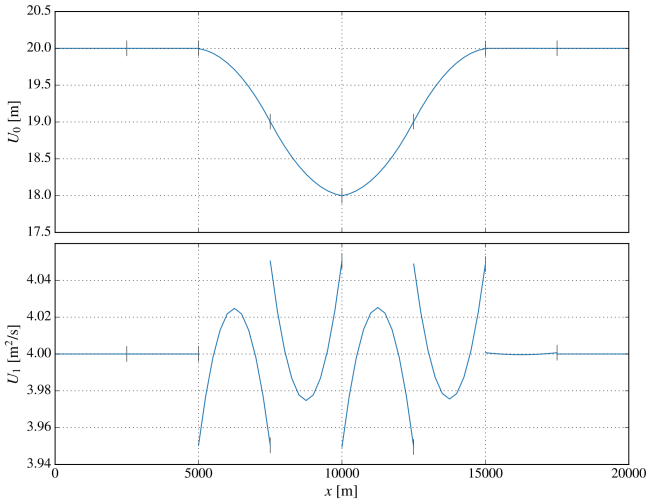

Figure B.1: Solution with 8 elements, the second order of polynomial and 2 Gauss-Legendre points, with a sinusoidal function.

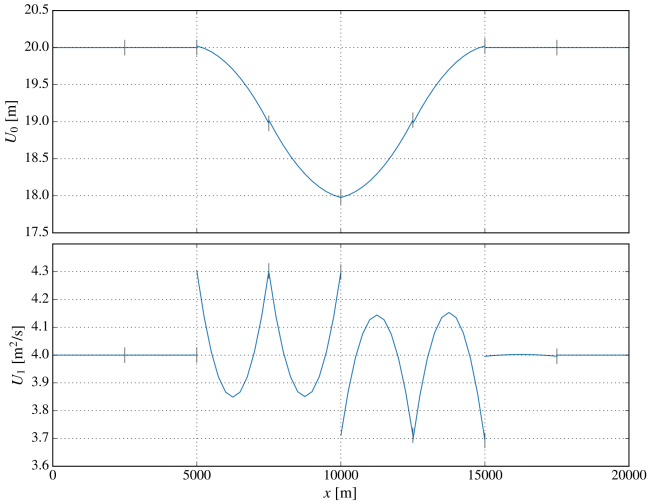

Figure B.2: Solution with 8 elements, the second order of polynomial and 4 Gauss-Legendre points, with a sinusoidal function.

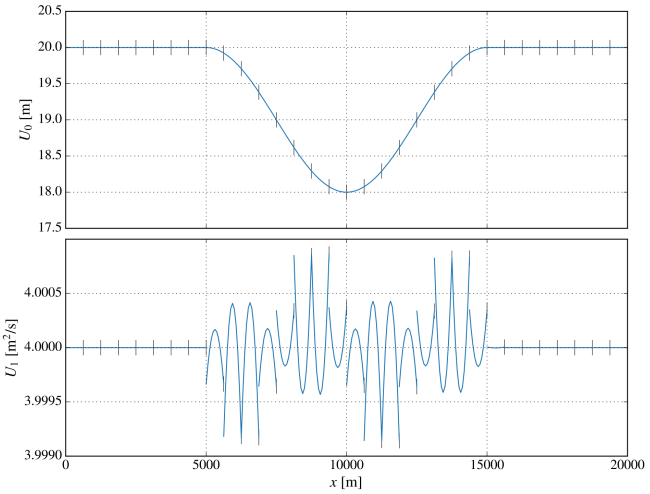

Figure B.3: Solution with 32 elements, the second order of polynomial and 2 Gauss-Legendre points, with a sinusoidal function.

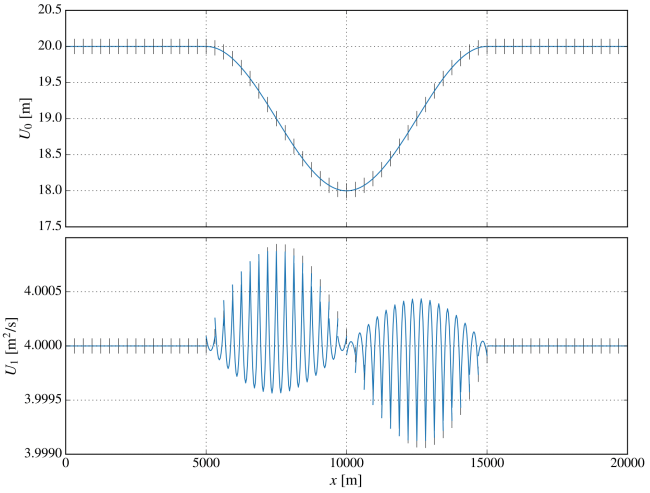

Figure B.4: Solution with 64 elements, the second order of polynomial and 4 Gauss-Legendre points, with a sinusoidal function.

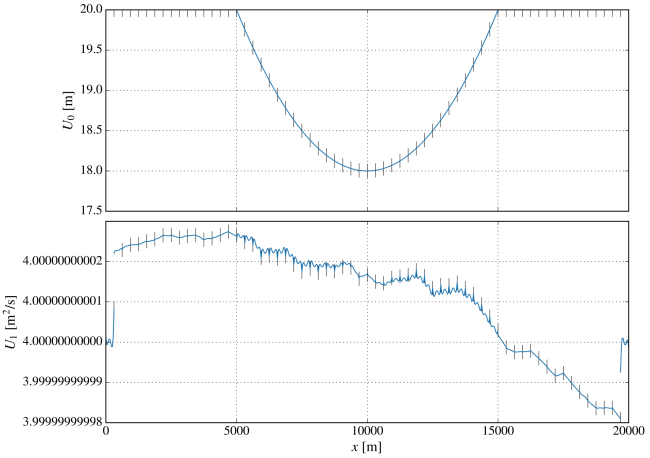

Figure B.5: Solution with 64 elements, the fourth order of polynomial and 7 Gauss-Legendre points.

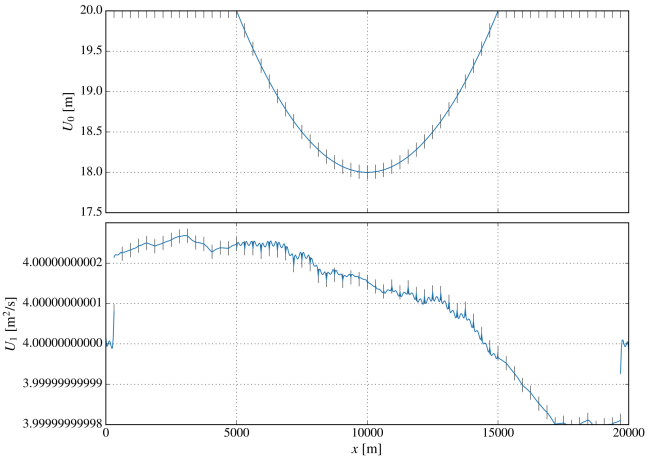

Figure B.6: Solution with 64 elements, the fourth order of polynomial and 8 Gauss-Legendre points.

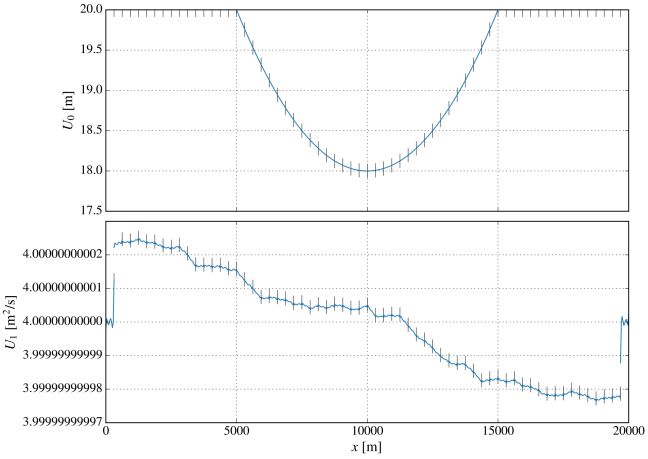

Figure B.7: Solution with 64 elements, the fifth order of polynomial and 8 Gauss-Legendre points.

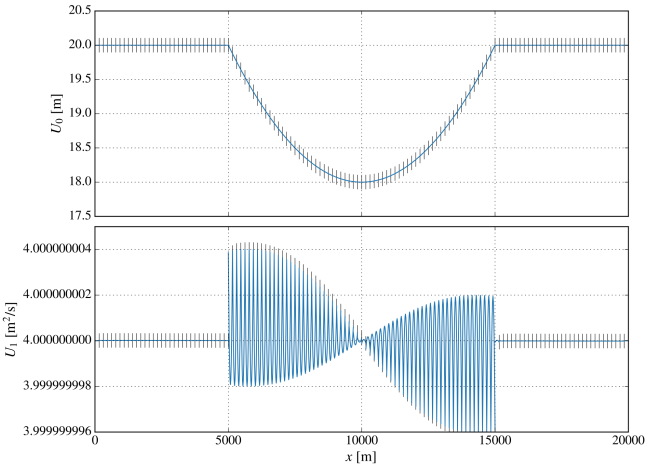

Figure B.8: Solution with 8 elements, the second order of polynomial and 3 Gauss-Legendre points, with a parabola function.

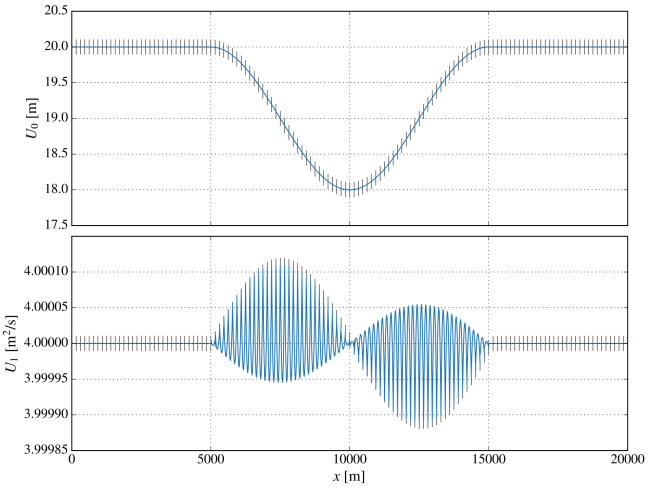

Figure B.9: Solution with 128 elements, the second order of polynomial and 4 Gauss-Legendre points, with a sinusoidal function.

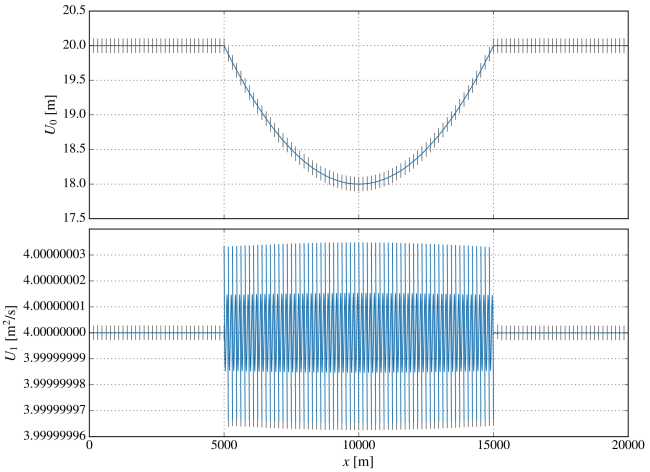

Figure B.10: Solution with 128 elements, the third order of polynomial and 3 Gauss-Legendre points.

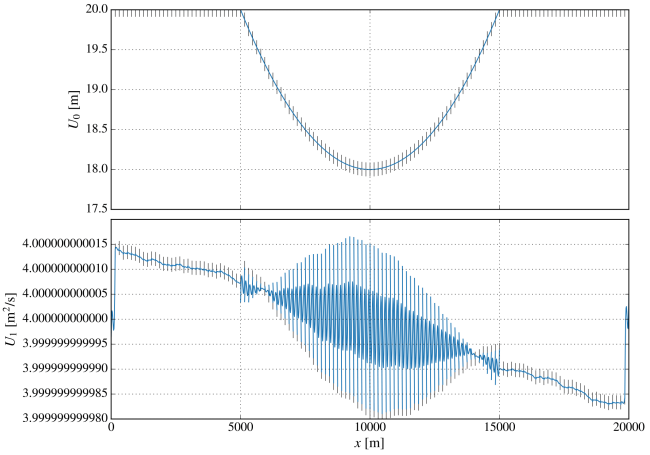

Figure B.11: Solution with 128 elements, the third order of polynomial and 5 Gauss-Legendre points.

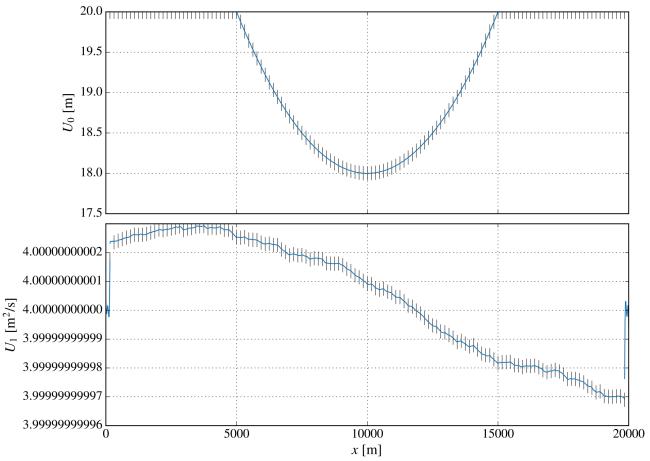

Figure B.12: Solution with 128 elements, the fourth order of polynomial and 8 Gauss-Legendre points.

Appendix C

Plots of the one-dimensional error

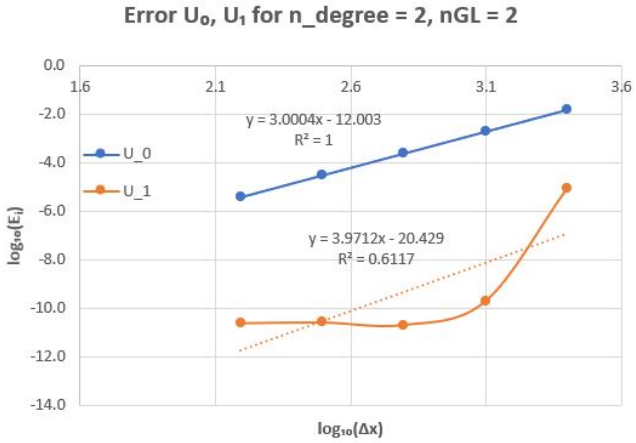

(a)

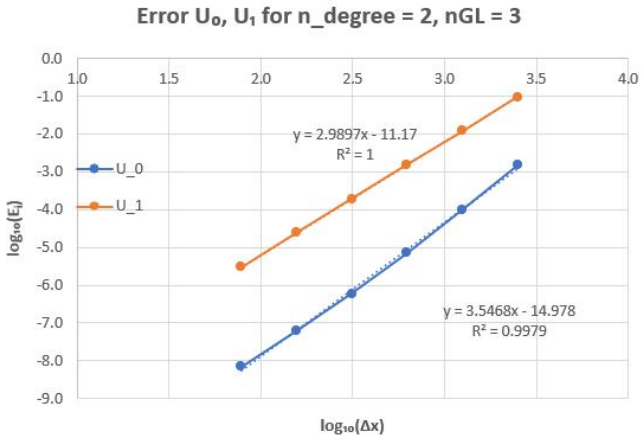

(b)

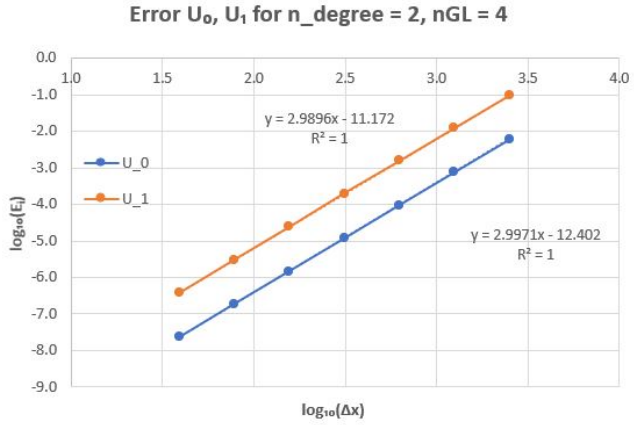

(c)

Figure C.1: Error of U_0 and U_1 with even numbers of elements, the second order of polynomial and a sinusoidal as bump function: (a) 2 Gauss-Legendre points, (b) 3 Gauss-Legendre points and (c) 4 Gauss-Legendre points.

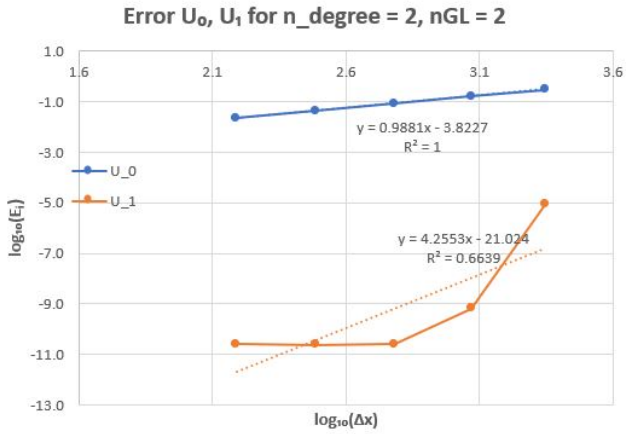

(a)

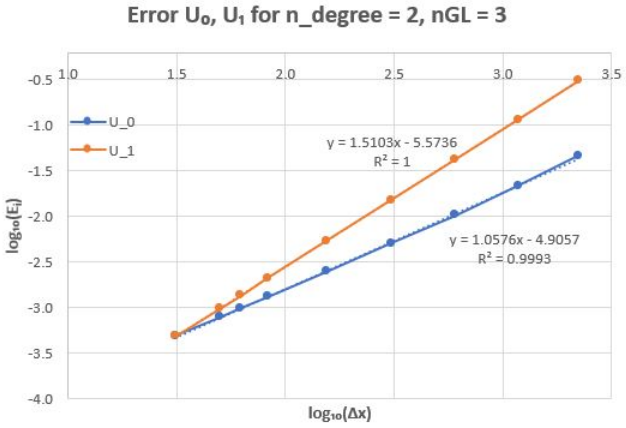

(b)

Figure C.2: Error of U_0 and U_1 with odd numbers of elements, the second order of polynomial and a parabola as bump function: (a) 2 Gauss-Legendre points and (b) 3 Gauss-Legendre points.

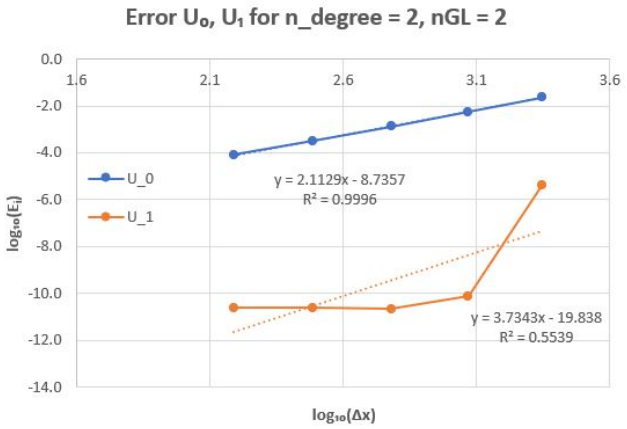

(a)

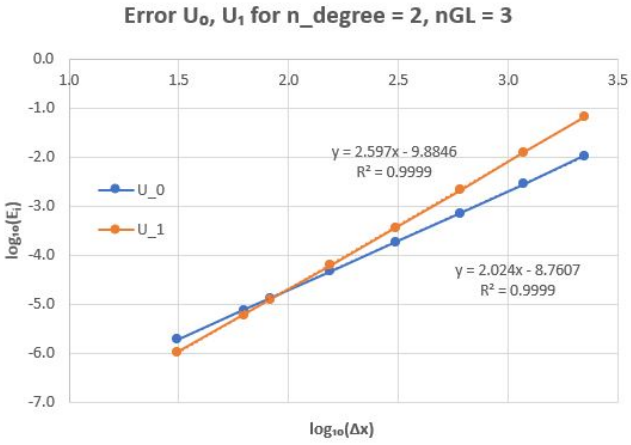

(b)

Figure C.3: Error of U_0 and U_1 with odd numbers of elements, the second order of polynomial and a sinusoidal as bump function: (a) 2 Gauss-Legendre points and (b) 3 Gauss-Legendre points.

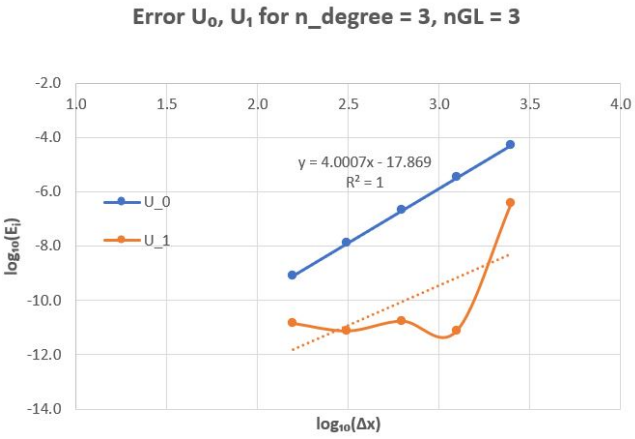

(a)

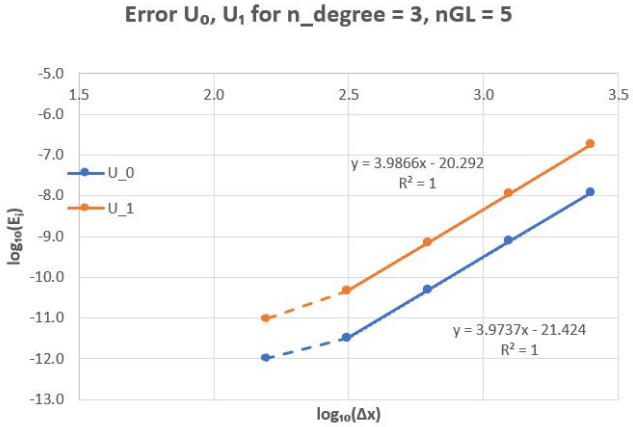

(b)

Figure C.4: Error of U_0 and U_1 with even numbers of elements, the third order of polynomial and a parabola as bump function: (a) 3 Gauss-Legendre points and (b) 5 Gauss-Legendre points.

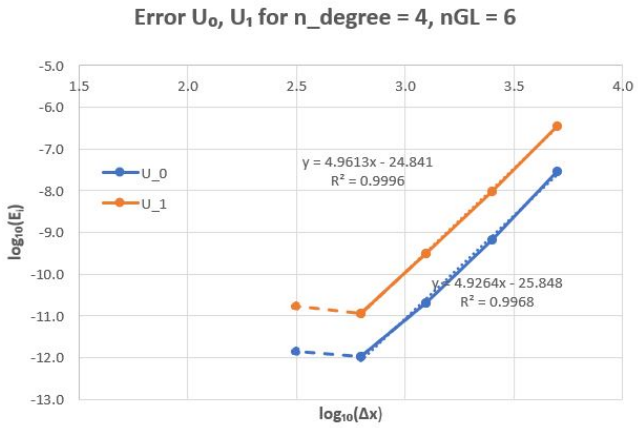

(a)

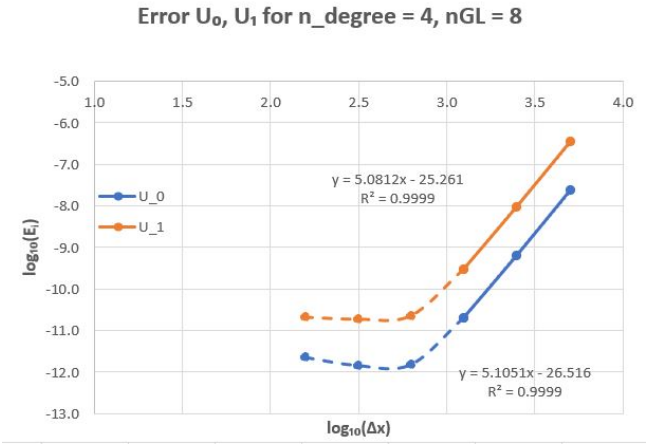

(b)

Figure C.5: Error of U_0 and U_1 with even numbers of elements, the fourth order of polynomial and a parabola as bump function: (a) 6 Gauss-Legendre points and (b) 8 Gauss-Legendre points.

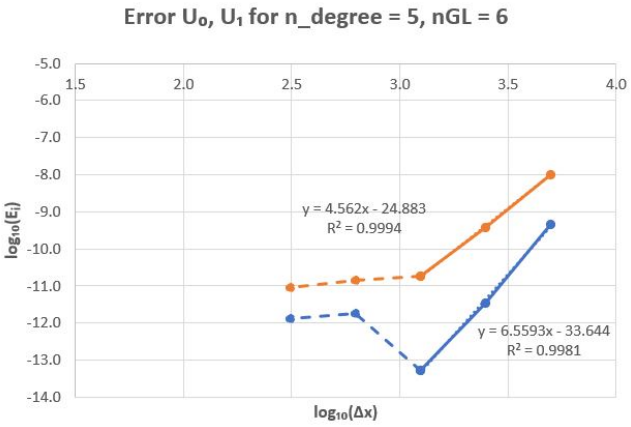

(a)

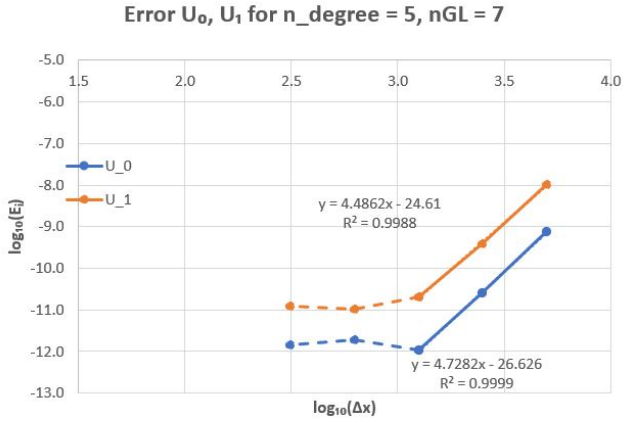

(b)

Figure C.6: Error of U_0 and U_1 with even numbers of elements, the fifth order of polynomial and a parabola as bump function: (a) 6 Gauss-Legendre points and (b) 7 Gauss-Legendre points.